UNIVERSITY
OF TRENTO

DEPARTMENT OF INFORMATION AND COMMUNICATION TECHNOLOGY

38050 Povo – Trento (Italy), Via Sommarive 14
http://www.dit.unitn.it

TOMOGRAPHIC SUB-SURFACE DETECTION OF DEFECTS BY MEANS OF A GA-BASED INVERSE SCATTERING PROCEDURE

M. Benedetti, M. Donelli, A. Massa, M. Pastorino, and A. Rosani

May 2005

Technical Report DIT-05-005

Tomographic Sub-Surface Detection of Defects by means of a GA-based Inverse Scattering Procedure

Manuel Benedetti, Massimo Donelli, Andrea Massa, Matteo Pastorino,* and Andrea Rosani

Department of Information and Communication Technologies,
University of Trento, Via Sommarive 14, 38050 Trento - Italy
Tel. +39 0461 882057, Fax +39 0461 882093
E-mail: *andrea.massa@ing.unitn.it,*
{*manuel.benedetti, massimo.donelli, andrea.rosani*}@*dit.unitn.it*

* Department of Biophysical and Electronic Engineering,
University of Genoa, Via Opera Pia 11/A, 16145 Genoa -Italy
Tel. +39 010 3532242, Fax +39 010 3532245
E-mail: *pastorino@dibe.unige.it*

Tomographic Sub-Surface Detection of Defects by means of a GA-based Inverse Scattering Procedure

Manuel Benedetti, Massimo Donelli, Andrea Massa, Matteo Pastorino, and Andrea Rosani

Abstract

In this paper, an assessment of the integrated genetic-algorithm strategy based on a numerically computed Green's function for subsurface inverse scattering problems arising in NDE/NDT industrial applications is presented. To show the effectiveness and current limitations of the approach in dealing with various scenarios characterized by lossless and lossy host media as well as in noisy environments, several numerical experiments are considered. The obtained results confirm the effectiveness of the approach in fully exploiting the available *a-priori* information through a suitable scattering model, which allows a non-negligible enhancement of the reconstruction accuracy as well as a reduction of the overall computational burden with respect to standard inverse scattering approaches.

Key words:

NDT/NDE, Industrial Process Tomography, Subsurface Microwave Imaging, Genetic Algorithm

1 Introduction

Subsurface sensing involves the detection, the localization, the discrimination, and the identification of unknown (or partially known) objects underneath and on a surface. Various applications of related technologies in many scientific and engineering branches can be taken into account. Let us consider the framework of non-destructive testing (NDT), civil constructions, railroads, maritime structures, mining, material inspection, surface metrology, geology, archeology, industrial process monitoring, etc.

Certainly, an area, which is strongly dependent on the development and application of advanced subsurface and surface sensing technologies, involves the detection and reconstruction (although limited to a set of characteristic parameters) of damages in industrial manufactures. This topic has received a great interest as both a major safety and economic concern. Considerable advances have been achieved in monitoring and detecting flaws and changes in structures thanks to the availability of wireless technologies, mems/micro/nano sensors and to the evolution of data post-processing techniques (e.g., data fusion, data management, etc..) allowing distributed sensing capabilities and quick structure recovering. As far as real-time monitoring is concerned, the development of advanced sensors [1] and the assessment of imaging techniques for the solution of the arising inverse scattering problem are key-issues to be further addressed.

In the framework of microwave imaging methods, several iterative inversion procedures have been proposed. From a computational point of view, these techniques can be grouped into two main categories according to the adopted optimization algorithm. The first one includes approaches based on local inversion algorithms [2]-[9]. The other considers global inversion procedures [10]-[13].

In general, whatever strategy, an imaging procedure is aimed at determining the object function in the overall investigation domain. However, such a requirement is unnecessary in industrial processes or material monitoring since a large portion of the investigation

domain is known. Thus it is profitable to develop customized inverse scattering approaches able to fully exploit the available *a-priori* information.

In [14], de Oliveira *et al.* developed an effective method for the eddy current evaluation of a defect in a conductive half-space by modelling the test zone as a distribution of cells either void or metallic and successively solving the arising optimization problems by means of a simulated annealing algorithm. The problem of low-frequency eddy current non-destructive evaluation of damaged metal structures has been also addressed in several papers through deterministic or stochastic techniques (see for example [15], [16], [17], and [18]).

Within the same framework, but considering microwave frequencies, Caorsi *et al.* [19] proposed a GA-based approach called "Free-space Green's function Approach" (FGA) where the defect was parameterized by a set of significant parameters to be determined during an iterative minimization process. In such a method, the reference background was assumed to be coincident with the free-space. Several numerical test cases confirmed the effectiveness of the approach in dealing with a free-space scenario or a weak host medium (in terms of dielectric characteristics), but also they highlighted the computational limitations of the FGA due to the large dimension of the unknowns array. To reduce the computational burden of the FGA (maintaining its key features), an improved microwave imaging procedure called "Inhomogeneous-space Green's function Approach" (IGA) has been recently presented [20]. A preliminary assessment has been performed by focusing on the relationship between the reconstruction accuracy and the crack's characteristics (dimensions and orientation).

In this paper, to complete the numerical validation, great care is devoted to determine the dependence of the retrieval capabilities of the IGA on the parameters and geometric features of the host medium where the defect is buried.

The manuscript is organized as follows. In Section 2 the subsurface inverse scattering problem arising in NDE/NDT industrial applications is presented and mathematically

formulated in terms of an optimization procedure, which considers a suitable scattering model based on a numerically computed inhomogeneous Green's function. Then, the iterative solution process based on a customized hybrid GA procedure is briefly resumed in Sect. 3 and assessed through a large set of numerical experiments aimed at pointing out the range of applicability of the approach (Sect. 4). Finally, some remarks and conclusions are reported (Sect. 5).

2 Mathematical Formulation

Let us consider the problem geometry shown in Figure 1(a). For the sake of simplicity, although much of the discussion also applies to a generic three-dimensional scenario, we refer in the following to the two-dimensional scalar case, $\underline{r} = (x, y)$. A cylindrical host object, with a known inhomogeneous cross section D_D, lies in an homogeneous background of dielectric characteristics $(\varepsilon_B, \sigma_B, \mu_B)$. The dielectric properties of D_D are $(\varepsilon_D, \sigma_D, \mu_D)$. A defect C is buried in the host medium. A set of V incident electromagnetic fields, $\underline{E}_v^{inc}(\underline{r})$, $v = 1, ..., V$, is used to sense the scatterer under test and a set of M measurement points are located according to a tomographic arrangement to collect scattered information.

A standard imaging process is aimed at reconstructing the dielectric properties of the object (and consequently, its shape and boundaries) by "*inverting*" the scattered data. The arising inverse scattering problem is usually heavily ill-posed. Moreover, the discretization of the whole cross section of the object requires a large number of unknowns making very difficult and computationally expensive an accurate reconstruction of the domain under test.

On the contrary, for the detection of subsurface cracks in a known configuration, the problem can be significantly simplified. Towards this end, let us define the following scattering potentials with respect to the external background

$$\gamma_C(\underline{r}) = \frac{1}{j2\pi f \varepsilon_B} \left\{ [\sigma_C(\underline{r}) - \sigma_B] + j2\pi f \varepsilon_B [\varepsilon_C(\underline{r}) - 1] \right\} \tag{1}$$

$$\gamma_D(\underline{r}) = \frac{1}{j2\pi f \varepsilon_B}\left\{[\sigma_D(\underline{r}) - \sigma_B] + j2\pi f \varepsilon_B [\varepsilon_D(\underline{r}) - 1]\right\} \quad (2)$$

where $(\varepsilon_C, \sigma_C)$ denote the relative dielectric permittivity and the conductivity of the crack C, respectively. Unlike imaging applications (Figure $1(b)$), the host medium is the "propagation medium" for the wave incident on the crack (Figure $1(c)$). Therefore, the scattered field can be computed through an integration limited to the area D_C occupied by the unknown defect. The computational saving is then evident by also considering that iterative solving procedures, requiring a forward computation at each iteration, are usually applied. More in detail, the scattered field, $\underline{E}_v^{scatt}(\underline{r}_m)$, $v = 1, ..., V$, $m = 1, ..., M$, and the internal total electric field, $\underline{E}_v^{tot}(\underline{r})$, $v = 1, ..., V$, are given by the well-known Fredholm integral equations of the first and second kind involving the proper Green's function [21]. In functional notation, these equations can be represented as follows

$$\Im_{IGA}\left\{\gamma(\underline{r}), \underline{E}_v^{tot}(\underline{r})\right\} - \underline{E}_v^{scatt}(\underline{r}_m) = 0 \quad m = 1, ..., M \quad v = 1, ..., V \quad (3)$$

$$\Re_{IGA}\left\{\gamma(\underline{r}), \underline{E}_v^{tot}(\underline{r})\right\} - \underline{E}_v^{inc}(\underline{r}) = 0 \quad v = 1, ..., V \quad (4)$$

where the sub-script "IGA" indicates the approach related to the Green's function for the inhomogeneous propagation medium. Moreover, equation (3) holds at the measurement points ($\underline{r} = \underline{r}_m$), whereas equation (4) holds inside C ($\underline{r} \in D_C$). The key point is the computation of the Green's function for the inhomogeneous configuration (Figure $1(c)$). Analytical forms for such a Green's function are available only for canonical objects [21][22]. However, the Green's function can be computed (according to its definition) as the forward solution of a direct scattering problem where a line current generates a field in the inhomogeneous configuration shown in Fig. $1(c)$. This can be accomplished in an effective way by using a suitable direct scattering method proposed in [23]. As an example, Figure 2 shows a pictorial representation of the Green's function for a source located at $x = y = -0.025\,\lambda$ and computed in a square two-dimensional domain of area $2.4\,\lambda \times 2.4\,\lambda$

containing an host medium $0.8\,\lambda$-sided. It should be noticed that such a computation is performed only-once for every host medium configuration and off-line. Therefore, the reconstruction process is concerned only with the crack area.

To avoid artifacts in the final reconstruction, the inverse problem is recast as an optimization one. This solution strategy has been widely investigated by several research teams (see, for example, [4][12] and the references cited therein). Present authors considered such an approach for imaging and NDT applications too, in which the whole cross section has been taken into account. The functional to be minimized can be defined as a measure of the fitting between actual and predicted data:

$$\psi\left\{\gamma\left(\underline{r}\right),\underline{E}_v^{tot}\left(\underline{r}\right)\right\}=\alpha\frac{\left\|\sum_{v=1}^{V}\sum_{m=1}^{M}\left[\Im_{IGA}\left\{\gamma(\underline{r}),\underline{E}_v^{tot}(\underline{r})\right\}-\underline{E}_v^{scatt}\left(\underline{r}_m\right)\right]\right\|}{\left\|\sum_{v=1}^{V}\sum_{m=1}^{M}\left[\underline{E}_v^{scatt}\left(\underline{r}_m\right)\right]\right\|}+\beta\frac{\left\|\sum_{v=1}^{V}\left[\Re_{IGA}\left\{\gamma(\underline{r}),\underline{E}_v^{tot}(\underline{r})\right\}-\underline{E}_v^{inc}(\underline{r})\right]\right\|}{\left\|\sum_{v=1}^{V}\left[\underline{E}_v^{inc}(\underline{r})\right]\right\|} \tag{5}$$

α and β being regularization constants usually chosen to obtain a good balance between the two terms of the functional and to take into account the reliability of measured data. In this framework, the IGA is effective in addressing the problem arising in NDE/NDT applications where the knowledge of the internal total electric field is not needed. However, except for the case of weakly scatterers [where the induced field can be approximated with the incident field (*Born approximation*)], the internal field is an unknown quantity as well as the scattering potential. Therefore, the possibility of reducing the "investigation region" to the current area of the crack (at each iteration of the optimization process) clearly allows a non-negligible time saving.

In order to minimize (5), ψ is discretized by considering a fixed partitioning of the host domain [24]. The crack is parametrized and assumed of simple shape (a rectangle). Center, dimensions and orientation are the unknowns of the buried defect and a subdomain of the host medium is assumed to belong to the crack when its center lies inside the rectangular perimeter of the defect. The problem is now to find

$$\chi_{opt} = arg\left(min_{\chi}\left[\Psi\left\{\chi\right\}\right]\right) \tag{6}$$

Ψ being the discretized counterpart of the functional (5) and where

$$\chi = \left\{x_C, y_C, w, \ell, \theta, \left[\xi^v_{n_C},\ n_C = 1, ..., N_C,\ v = 1, ..., V\right]\right\} \tag{7}$$

is the array of unknown parameters, $\xi^v_{n_C}$ being the value of the total electric field at the center of the n_c-th cell of the crack for the v-th illumination (the scalar nature of the field unknowns comes from the assumption of a TM-type illumination). Moreover, (x_C, y_C) indicate the center of the crack, w and ℓ its linear dimensions, and θ the orientation of the defect.

Since the optimization approach is iterative, all the unknown parameters depends on the iteration step k. Therefore, the variable dimension of the array $\chi^{(k)}$ is given by the parameters of the crack and the field unknowns $(N_C^{(k)} \times V)$, $N_C^{(k)}$ being the number of subdomains whose centers belong to the estimated area of the defect at the k-th iteration. The minimization process is performed iteratively by applying a suitable hybrid-coded genetic algorithm as briefly resumed in the following section and detailed in [20].

3 Minimization Procedure

A key issue of the proposed approach is the optimization of the unknown array. After the discretization of the investigation domain in a grid of N square sub-domains, χ turns out to be a combination of integer (i.e., the coordinates of the center of the crack, the crack length, its width and its orientation expressed as an integer function of the side of the discretization sub-domain) and real-valued quantities (i.e., the values of the total electric field).

As it usually becomes in standard GAs, starting from the original optimization space of *phenotypes*, the problem is reformulated in the *genotype* space where all the genetic operations take place. Even tough a standard GA considers a binary-coded format of

the *chromosome* (i.e., the representation of the unknown array in the genotype space), because of the hybrid nature of the unknown array χ, a mixed binary/floating-point representation $\aleph$ is used

$$\aleph = \left\{ b_1^{(x_C)}, ..., b_C^{(x_C)}; b_1^{(y_C)}, ..., b_C^{(y_C)}; b_1^{(w)}, ..., b_R^{(w)}; b_Q^{(\ell)}, ..., b_Q^{(\ell)}; b_T^{(\theta)}, ..., b_T^{(\theta)}; \left[\xi_{n_C}^v,\ n_C = 1, ..., N_C,\ v = 1, ..., V \right] \right\} \tag{8}$$

where $b_i^{(j)}$ is the i-th bit related to the j-th parameter, $C = log_2 N_l$ ($N_l = \sqrt{N}$), $Q = log_2 L$, $R = log_2 W$, and $T = log_2 P$. C, Q, T, and R being the number of values that the discrete variable x_C and y_C, w, ℓ, θ can assume, respectively.

Accordingly, the fundamental genetic mechanisms differ from those commonly encountered in the literature and customized crossover and mutation must be defined. Nevertheless, the mutation always produces a modification of the population characteristics by introducing new genetic material and the crossover remains a method for merging the features of the individuals.

More in detail, the mutation operators are defined according to [19] and the crossover is modified to deal with a variable-length chromosome $\aleph$. In particular, when the cross-position lies into the binary part of the chromosome and the defect of the produced offspring occupies a number of sub-domains equal to or smaller than that occupied by one of their parent $\aleph_{q_1}^{(k)}$, $\aleph_{q_2}^{(k)}$ then

$$\begin{array}{l} \left\{ \xi_{n_C}^v \right\}_{q_1}^{(k+1)} = \frac{r \left\{ \xi_{n_C}^v \right\}_{q_1}^{(k)} + (1-r) \left\{ \xi_{n_C}^v \right\}_{q_2}^{(k)}}{2}, \quad n_C = 1, ..., \{N_C\}_{q_1}^{(k+1)} \\ \left\{ \xi_{n_C}^v \right\}_{q_2}^{(k+1)} = \frac{(1-r) \left\{ \xi_{n_C}^v \right\}_{q_1}^{(k)} + r \left\{ \xi_{n_C}^v \right\}_{q_2}^{(k)}}{2}, \quad n_C = 1, ..., \{N_C\}_{q_2}^{(k+1)} \end{array} \quad \{N_C\}_{q_a}^{(k+1)} \leq max_b \left(\{N_C\}_{q_b}^{(k)} \right) \tag{9}$$

$r \in [0, 1]$ being a random number. Otherwise, if $\{N_C\}_{q_a}^{(k+1)} > max_b \left(\{N_C\}_{q_b}^{(k)} \right)$, a, $b = 1, 2$, then $\left\{ \xi_{n_C}^v \right\}_{q_a}^{(k+1)}$; $n_C = \left(max_b \{N_C\}_{q_b}^{(k)} + 1 \right), ..., \{N_C\}_{q_a}^{(k+1)}$ is fixed to the value of the electric field at the same n_C-th cell of the crack-free scenario, $\zeta_{n_C}^v$.

On the other hand, when the crossover-point lies at the position $n_C = n_{cross}$ into the

real part of the chromosome and $\{N_C\}_{q_a}^{(k)} > \{N_C\}_{q_b}^{(k)}$, $a \neq b$, the real-parts of the new chromosomes are modified as follows

$$\left\{\xi_{n_C}^v\right\}_{q_b}^{(k+1)} = \begin{cases} \left\{\xi_{n_C}^v\right\}_{q_b}^{(k)} \left\{E_{tot}^v\left(x_p, y_p\right)\right\}_{q_b}^{(h)} & n_C = 1, ..., n_{cross} \\ \left\{\xi_{n_C}^v\right\}_{q_a}^{(k)} \left\{E_{tot}^v\left(x_p, y_p\right)\right\}_{q_a}^{(h)} & n_C = \left(n_{cross}+1\right), ..., \{N_C\}_{q_b}^{(k)} \end{cases} \tag{10}$$

$$\left\{\xi_{n_C}^v\right\}_{q_a}^{(k+1)} = \begin{cases} \left\{\xi_{n_C}^v\right\}_{q_a}^{(k)} & n_C = 1, ..., n_{cross} \\ \left\{\xi_{n_C}^v\right\}_{q_b}^{(k)} & n_C = \left(n_{cross}+1\right), ..., \{N_C\}_{q_b}^{(k)} \\ \zeta_{n_C}^v & n_C = \left(\{N_C\}_{q_b}^{(k)}+1\right), ..., \{N_C\}_{q_a}^{(k)} \end{cases} \tag{11}$$

Finally, to allow that the solution can only improve over the course of the genetic evolution, a standard *elitist* strategy is implemented over the generations.

4 Numerical Results

In this section, the results of several numerical simulations are reported. Concerning the notation, the following geometrical parameters are used:

- A_D and A_C denote the area of the host medium and of the crack, respectively;
- x_C and y_C are the cartesian coordinates of the crack's center.

Moreover, symbols $\hat{A}_D$, $\hat{A}_C$, $\hat{x}_C$, and $\hat{y}_C$ are adopted to indicate the estimated quantities. To evaluate the effectiveness of the IGA method and its better performance with respect to the FGA technique, a reference geometry has been considered where a square host medium includes a square defect.

In all experiments, the following values of GAs' parameters have been assumed. The population size was set to $P = 80$, the maximum number of generations was equal to $K = 200$, and the crossover and mutation rates was $P_c = 0.7$ and $P_m = 0.05$, respectively. These values arose from a large set of experiments and they are in line with reference parameters encountered in literature on the subject [25], [26].

The numerical results have been evaluated in terms of the following quantitative error figures: the *defect-localization error* δ_C

$$\delta_C = \frac{\sqrt{(x_C - \widehat{x}_C)^2 + (y_C - \widehat{y}_C)^2}}{d_{max}} \times 100 \tag{12}$$

and the *defect-dimension error*

$$\delta_A = \left| \frac{A_C - \widehat{A}_C}{A_C} \right| \times 100 \tag{13}$$

. Moreover, since simulated measurements using a forward solver with the actual parameters have been generated instead carrying out real experiments, a Gaussian-noise has been successively added to simulate experimentally acquired data that are corrupted with a measurement noise.

In the "Test Case 1", the effect of the dimension of the host medium has been evaluated. The first experiment deals with a void square defect located at $x_C = 0.15\,\lambda$ and $y_C = 0.10\,\lambda$ of area $A_C = 0.04\,\lambda^2$ and lying in a lossless host medium $\sigma_D = 0.0$ ($\varepsilon_D = 2.0$). Figure 3 gives the obtained values of the error figures in the range $0.25 \leq \frac{A_D}{\lambda^2} \leq 2.25$ and when $2.5\,dB \leq SNR \leq 30\,dB$ [Figs. 3(a)-3(c)]. For comparison purposes, the same quantities concerning the FGA are reported in Figs. 3(b) and 3(d). As expected, when the value of A_D is small, the localization of the crack is quite good and it slightly deteriorates for smallest values of SNR. However, while the localization accuracy of the FGA is significantly affected by the dimension of the host medium, the IGA performs very efficiently at least for the highest values of SNR[(1)]. As an example, Figures 3(e) and 3(f) show the quantitative behavior of δ_C and δ_A versus A_D for a fixed value of the signal-to-noise ratio ($SNR = 13.75\,dB$). Moreover, for $\frac{A_D}{\lambda^2} = 1.25$, Figures 3($g$) and 3($h$)

(1) It should be observed that the 3D plots of Fig. 3 (as well as the following ones) are not smooth due to the rather limited number of repeated tests for each combination of $\frac{A_D}{\lambda^2}$ and SNR (because of the stochastic nature of the approach as well as of the noise, ten simulations have been run for each configuration).

give the values of the error figures for different SNRs. Except for highest noise levels, taking into account the Green's function of the host medium results in better defect's retrievals. Clearly, for $SNR \approx 2.5\,dB$, the noise level is such that the positive effect of the use of the inhomogeneous Green's function is completely ruined.

In the second experiment, the impact of the ratio between the permittivity of the host medium and that of the defect has been evaluated. For these simulations, the following configuration has been assumed: $\frac{A_D}{A_C} = 28.45$, $x_C = 0.15\,\lambda$, $y_C = 0.10\,\lambda$, $\sigma_C = 0.0$, $\sigma_D = 1.0\,\frac{S}{m}$, and $SNR = 15\,dB$.

Figure 4 reports the obtained results. For the lowest values of ε_C, IGA still overcomes the FGA, whereas the behaviors of the error figures turns out to be irregular since the defect constitutes alternately a weak or a strong scatterer with a dielectric permittivity relative to the host medium ($\frac{\varepsilon_C}{\varepsilon_D}$) sometimes ≥ 1 and sometimes < 1. The same irregular behavior is present in the plots of δ_A, as well. However, in such a case, larger errors occur when the FGA is applied for the highest values of ε_D and ε_C.

The above interesting behavior can be better noticed from Figures $4(e)$-(f) and Figures $4(g)$-(e), which show the error figures δ_C and δ_A, for $\varepsilon_D = 3.0$ and $1.0 \leq \varepsilon_C \leq 5.0$, and for $1.0 \leq \varepsilon_D \leq 5.0$ and $\varepsilon_C = 3.0$, respectively.

The same simulations have been repeated for different noisy environments. In such experiments, $\frac{A_D}{A_C} = 16.0$, $x_C = 0.26\,\lambda$, $y_C = 0.0$, $\varepsilon_C = 1.0$, and $\sigma_C = 0.0$. In all cases [Figs. $5(a)$-(d)], the IGA performs better than the FGA and its behavior is less sensitive to the noise superimposed to the input data. Specific quantitative considerations, pointing out the advantages of the IGA method, can be drawn from Figures $5(e)$-(h) concerning the particular cases in which $SNR = 13.75\,dB$ with $1.0 \leq \varepsilon_D \leq 5.0$, and $\varepsilon_D = 3.0$ with $2.5\,dB \leq SNR \leq 30\,dB$.

Successively, lossy materials have been considered. The working frequency has been fixed to $f = 6\,GHz$ and different configurations have been analyzed ($0.0\,\frac{S}{m} \leq \sigma_C \leq 1.0\,\frac{S}{m}$ and $0.0\,\frac{S}{m} \leq \sigma_D \leq 1.0\,\frac{S}{m}$). Figure 6 shows the reconstruction results when $\frac{A_D}{A_C} = 16.0$,

$x_C = 0.15\,\lambda$, $y_C = 0.10\,\lambda$, $\varepsilon_C = 1.0$, $\varepsilon_D = 2.0$, and $SNR = 15.0\,dB$. As expected, the accuracy in computation of the inhomogeneous Green's function is far less than in lossless case, since the solution of a forward scattering problem, which involves strong attenuations along paths connecting source and field points, is required. Such difficulties are confirmed by the rather complex behaviors of the error figures, which do not guarantee that the IGA outperforms the FGA at all if the electric conductivity is not enough small. Finally, as an example of the typical behavior of the reconstruction process, Figure 7 compares the retrieved images at different iterations when the FGA [Figs. $7(a)(c)(e)(g)$] and the IGA are applied [Figs. $7(b)(d)(f)(h)$] ($\frac{A_D}{A_C} = 28.44$, $x_C = 0.15\,\lambda$, $y_C = 0.10\,\lambda$, $\varepsilon_C = 3.5$, $\sigma_C = 0.0$, $\varepsilon_D = 1.5$, $\sigma_D = 0.1\,\frac{S}{m}$, and $SNR = 15.0\,dB$). As a reference, the actual profile is also reported [Fig. $7(i)$].

5 Conclusions

In this paper, an inverse-scattering-based procedure for the detection of buried defects has been studied. The host medium, which includes the defect, is inspected by means of interrogating microwaves. The problem solution is recast as an optimization problem, which is solved through a customized genetic algorithm. The key-point of the approach is the use of an integrated genetic-algorithm strategy based on a numerically computed Green's function for the inhomogeneous configuration constituted by the host medium in the external homogeneous background. Such a methodological approach represents a direct way to include *a-priori* information into the scattering model and it allows a non-negligible enhancement of the reconstruction accuracy as well as a reduction of the overall computational burden.

Several numerical results have been reported, concerning noiseless as well as noisy environments with lossless and lossy materials to evaluate the effectiveness of the method in dependence on the characteristics of the host medium. As a matter of fact, such an anal-

ysis completes the assessment of the proposed technique presented in [20] and focused on the relationship between performance and properties and dimension of the defect. Moreover, for comparison purposes, the method has been compared with a more classic approach based on the free-space Green's function, which needs to take into account the complete investigation domain by requiring large computational resources and computer memory.

References

[1] E. Nyfors, "Industrial microwave sensors - A review," *Subsurface Sensing Technologies and Applications*, vol. 1, pp. 23-43, 2000.

[2] M. Moghaddam and W. C. Chew, "Study of some practical issues in inversion with the Born iterative method using time-domain data," *IEEE Trans. Antennas Propagat.*, vol. 41, pp. 177-184, 1993.

[3] W. C. Chew and Y. M. Wang, "Reconstruction of two-dimensional permittivity using the distorted Born iterative method," *IEEE Trans. Med. Imag.*, vol. 9, pp. 218-225, 1990.

[4] A. Franchois and Ch. Pichot, "Microwave imaging - Complex permittivity reconstruction with a Levenberg-Marquardt method," *IEEE Trans. Antennas Propagat.*, vol. 45, pp. 203-215, 1997.

[5] N. Joachimowicz, J. J. Mallorqui, J.-C. Bolomey, and A. Broquetas, "Convergence and stability assessment of Newton-Kantorovich reconstruction algorithms for microwave tomography," *IEEE Trans. Medical Imaging*, vol. 17, pp. 562-570, 1998.

[6] R. E. Kleinman and P. M. van den Berg, "A modified gradient method for two-dimensional problems in tomography," *J. Comput. Appl. Math.*, vol. 42, pp. 17-35, 1992.

[7] H. Harada, D. J. N. Wall, T. Takenaka, and M. Tanaka, "Conjugate gradient method applied to inverse scattering problem," *IEEE Trans. Antennas Propagat.*, vol. 43, pp. 784-792, 1995.

[8] T. Isernia, V. Pascazio, and R. Pierri, "A nonlinear estimation method in tomographic imaging," *IEEE Trans. Geosci. Remote Sensing*, vol. 35, pp. 910-923, 1997.

[9] P. M. van den Berg and A. Abubakar, "Contrast source inversion: state of art," *Progress in Electromagnetic Research*, vol. 34, pp. 189-218, 2001.

[10] Z. Q. Meng, T. Takenaka, and T. Tanaka, "Image reconstruction of two-dimensional impenetrable objects using genetic algorithms," *J. Electromagn. Waves Applicat.*, vol. 13, pp. 95-118, 1999.

[11] S. Caorsi, A. Massa, and M. Pastorino, "A computational technique based on a real-coded genetic algorithm for microwave imaging purposes," *IEEE Trans. Geosci. Remote Sensing*, vol. 38, pp. 1679-1708, 2000.

[12] A. Massa, "Genetic-algorithm-based techniques for 2D microwave inverse scattering," in *Recent Research Developments in Microwave Theory and Techniques*, Transworld Res. Network Press, Trivandrum, India, 2002.

[13] J. W. Ra, H. K. Choi, and J. S. Kim, "Two-and-half dimensional reconstruction of buried tunnel and pipes from cross-borehole and reflection measurements by using a genetic and Levenburg-Marquardt hybrid algorithm," *Inverse Problems*, vol. 17, pp. 233-252, 2003.

[14] R. de Oliveira, D. Lesselier, and B. Duchene, "Mapping defects in a conductive half-space by simulated annealing with connectivity and size as constraints," *J. Electrom. Waves Applicat.*, vol. 10, pp. 983-1004, 1996.

[15] A. A. Arkadan, Y. Chen, S. Subramaniam, and S. R. H. Hoole, "NDT identification of a crack using ANNs with stochastic gradient descent," *IEEE Trans. Magn.*, vol. 31, pp. 1984-1987, 1995.

[16] S. Norton and J. Bowler, "Theory of eddy current inversion," *J. Appl. Phys.*, vol. 73, pp. 501-512, 1993.

[17] R. Zorgati, B. Duchene, D. Lesselier, and F. Pons, "Eddy current testing of anomalies in conductive materials, Part I: Qualitative imaging via diffraction tomography technique," *IEEE Trans. Magn.*, vol. 27, pp. 4416-4437, 1991.

[18] R. Zorgati, B. Duchene, D. Lesselier, and F. Pons, "Eddy current testing of anomalies in conductive materials, Part II: Quantitative imaging via generalized inverse techniques," *IEEE Trans. Magn.*, vol. 28, pp. 1850-1862, 1992.

[19] S. Caorsi, A. Massa, and M. Pastorino, "A crack identification microwave procedure based on a genetic algorithm for non-destructive testing," *IEEE Trans. Antennas Propagat.*, vol 49, pp. 1812-1820, Dec. 2001.

[20] S. Caorsi, A. Massa, M. Pastorino, and M. Donelli, "Improved microwave imaging procedure for non-destructive evaluations of two-dimensional structures," *IEEE Trans. Antennas Propagat.*, vol. 52, pp.1386-1396, Jun. 2004.

[21] C. T. Tai, *Dyadic Green's Function in Electromagnetic Theory.* Intex Publishers, New York, 1971.

[22] J. Van Bladel, *Electromagnetic Fields.* McGraw-Hill , New York, 1964.

[23] S. Caorsi, G. L. Gragnani, M. Pastorino, and M. Rebagliati, "A model-driven approach to microwave diagnostics in biomedical applications," *IEEE Trans. Microwave Theory Tech.*, vol. 44, pp. 1910-1920, 1996.

[24] J. H. Richmond, "Scattering by a dielectric cylinder of arbitrary cross section shape," *IEEE Trans. Antennas Propagat.*, vol. 13, pp. 334-341, 1965.

[25] D. E. Goldberg, "Real-coded genetic algorithms, virtual alphabets, and blocking," *Complex Syst.*, vol. 5, pp. 139-167, 1991.

[26] Z. Michalewicz, *Genetic Algorithms + Data Structures = Evolution Programs.* Springer-Verlag, Berlin, 1996.

FIGURE CAPTIONS

- Figure 1.

  Original Problem - (a) Problem geometry. *Equivalent problem* - (b) Free-space Green's function: background scenario, (c) Inhomogeneous Green's function: background scenario.

- Figure 2.

  Numerically computed inhomogeneous Green's function for a source located at $\frac{x}{\lambda} = \frac{y}{\lambda} = -0.025$ of the host medium characterized by: (a) $\sigma_D = 0.0$, $\varepsilon_D = 1.0$ (Free space Green's function), (b) $\sigma_D = 0.0$, $\varepsilon_D = 2.0$, (c) $\sigma_D = 0.0$, $\varepsilon_D = 5.0$, (d) $\sigma_D = 0.1$, $\varepsilon_D = 2.0$, (e) $\sigma_D = 0.5$, $\varepsilon_D = 2.0$, and (f) $\sigma_D = 1.0$, $\varepsilon_D = 2.0$.

- Figure 3.

  Reconstruction accuracy versus host-medium extension A_D for different SNR values: $(a)(b)$ localization error, δ_C, and $(c)(d)$ error in the crack-area estimation, δ_A. $(a)(c)$ IGA and $(b)(d)$ FGA procedures. Behaviors of δ_C (e) and δ_A (f) versus $\frac{A_D}{\lambda^2}$ when $SNR = 13.75\,dB$. Behaviors of δ_C (g) and δ_A (h) versus SNR when $\frac{A_D}{\lambda^2} = 1.25$.

- Figure 4.

  Dependence of the reconstruction accuracy on dielectric characteristics ratio ($SNR = 15\,dB$) - Impact of the dielectric permittivity ratio, $\left(\frac{\varepsilon_C}{\varepsilon_D}\right)$: $(a)(b)$ localization error, δ_C, and $(c)(d)$ error in the crack-area estimation, δ_A. $(a)(c)$ IGA and $(b)(d)$ FGA procedures. Behaviors of δ_C (e) and δ_A (f) versus ε_C when $\varepsilon_D = 3.0$. Behaviors of δ_C (g) and δ_A (h) versus ε_D when $\varepsilon_C = 3.0$.

- Figure 5.

  Reconstruction accuracy versus dielectric characteristics of the host medium for different SNR values - Impact of the electric conductivity of the host medium,

σ_D: $(a)(b)$ localization error, δ_C, and $(c)(d)$ error in the crack-area estimation, δ_A. $(a)(c)$ FGA and $(b)(d)$ IGA procedures. Behaviors of δ_C (e) and δ_A (f) versus ε_D when $SNR = 13.75\,dB$. Behaviors of δ_C (g) and δ_A (h) versus SNR when $\varepsilon_D = 3.0$.

- Figure 6.

  Dependence of the reconstruction accuracy on dielectric characteristics ratio ($SNR = 15\,dB$) - Impact of the electric conductivity ratio, $\left(\frac{\sigma_C}{\sigma_D}\right)$: $(a)(b)$ localization error, δ_C, and (c)-(d) error in the crack-area estimation, δ_A. $(a)(c)$ FGA and $(b)(d)$ IGA procedures. Behaviors of δ_C (e) and δ_A (f) versus σ_C when $\sigma_D = 0.5\,\frac{S}{m}$. Behaviors of δ_C (g) and δ_A (h) versus σ_D when $\sigma_C = 0.5\,\frac{S}{m}$.

- Figure 7.

  Evolution of the crack detection and reconstruction ($SNR = 15\,dB$) at the iteration $(a)(b)$ $k = 1$, $(c)(d)$ $k = 50$, $(e)(f)$ $k = 100$, $(g)(h)$ $k = k*$. Actual configuration (i). $(a)(c)(e)(g)$ FGA and $(b)(d)(f)(h)$ IGA procedures.

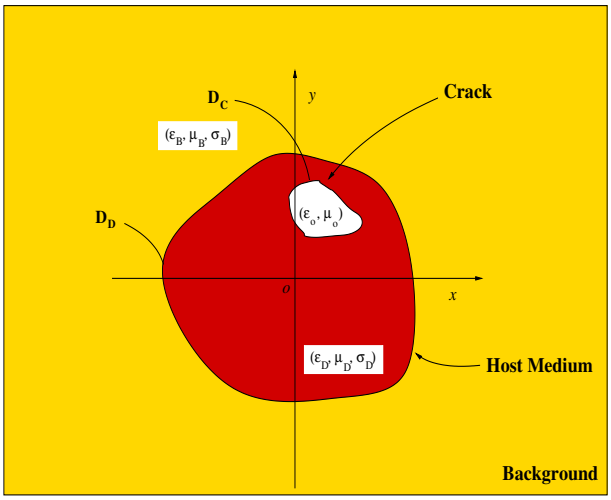

(a)

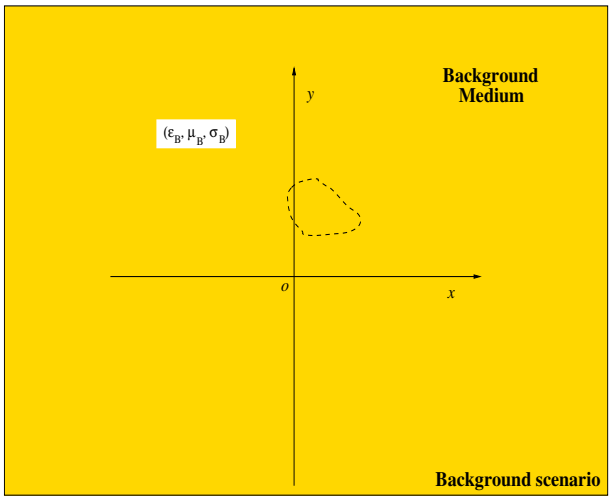

(b)

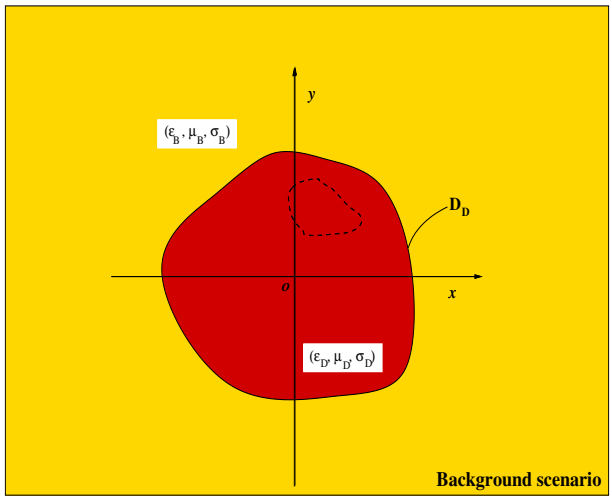

(c)

Fig. 1 - M. Benedetti *et al.*, "Tomographic Sub-Surface Detection ..."

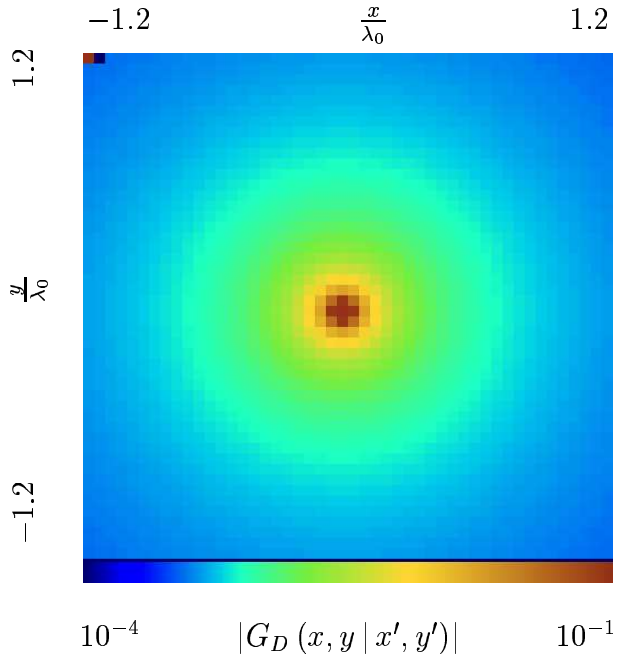

(a)

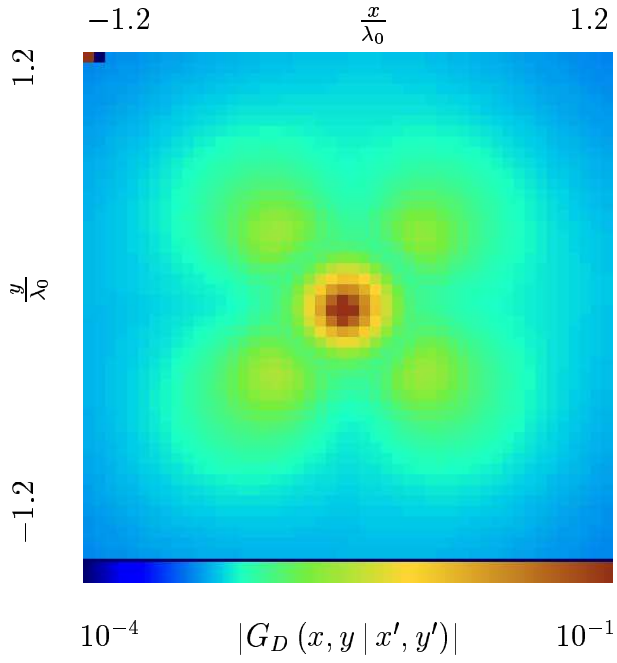

(b)

Fig. 2(*I*) - M. Benedetti *et al.,* "Tomographic Sub-Surface Detection ..."

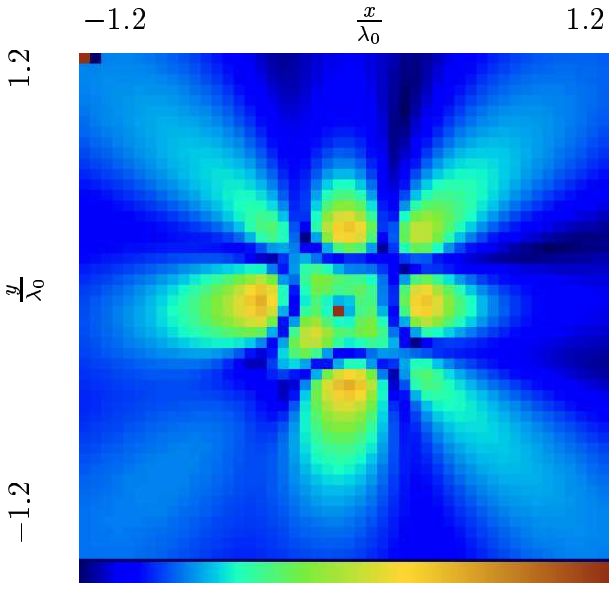

(c)

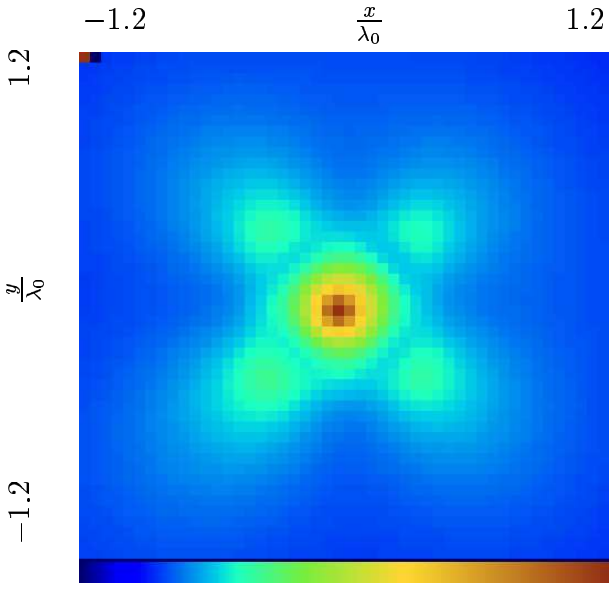

(d)

Fig. 2(*II*) - M. Benedetti *et al.,* "Tomographic Sub-Surface Detection ..."

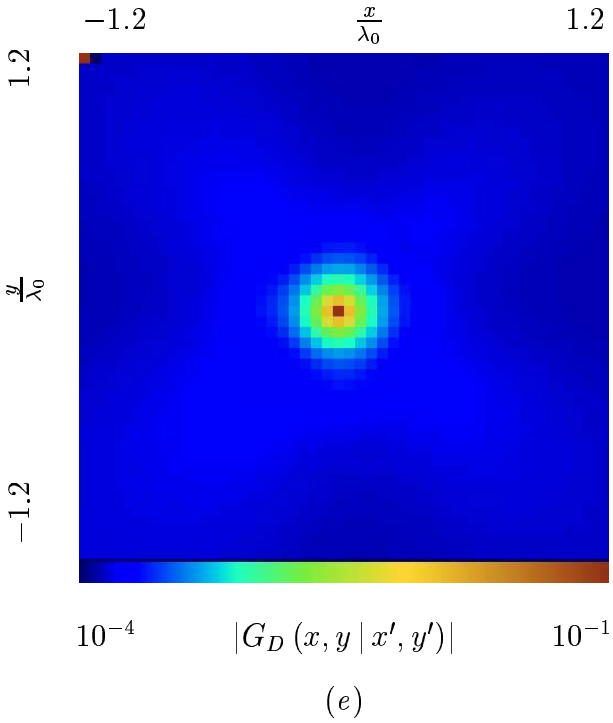

(e)

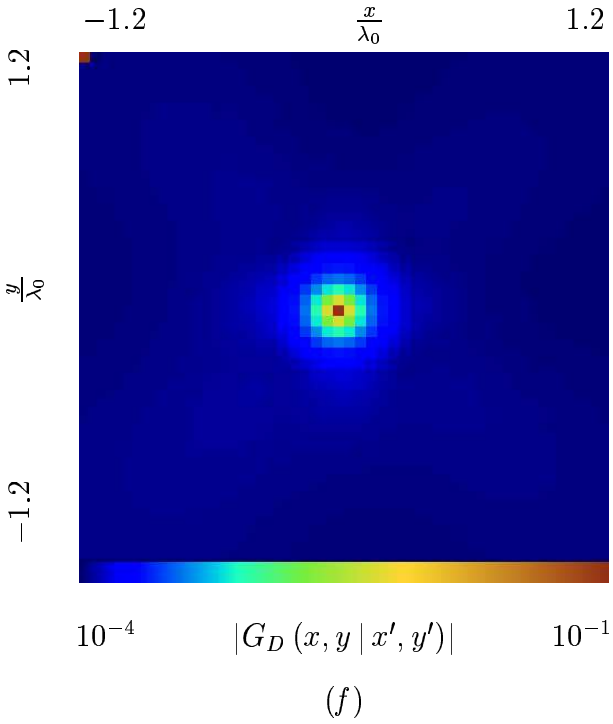

(f)

Fig. 2(*III*) - M. Benedetti *et al.,* "Tomographic Sub-Surface Detection ..."

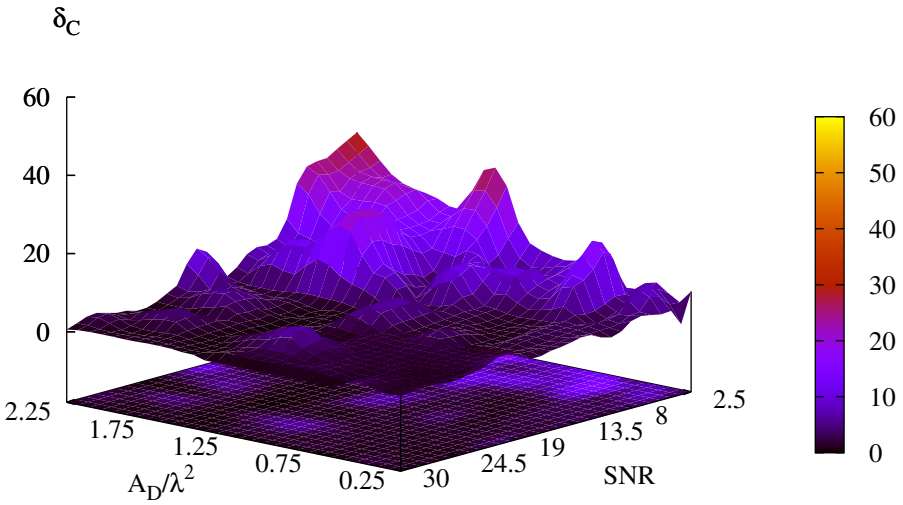

(*a*)

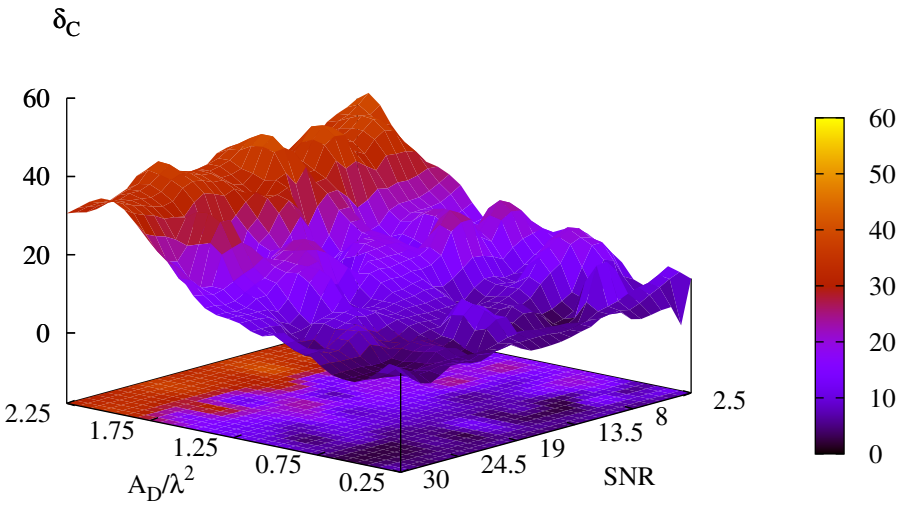

(*b*)

Fig. 3(*I*) - M. Benedetti *et al.*, "Tomographic Sub-Surface Detection ..."

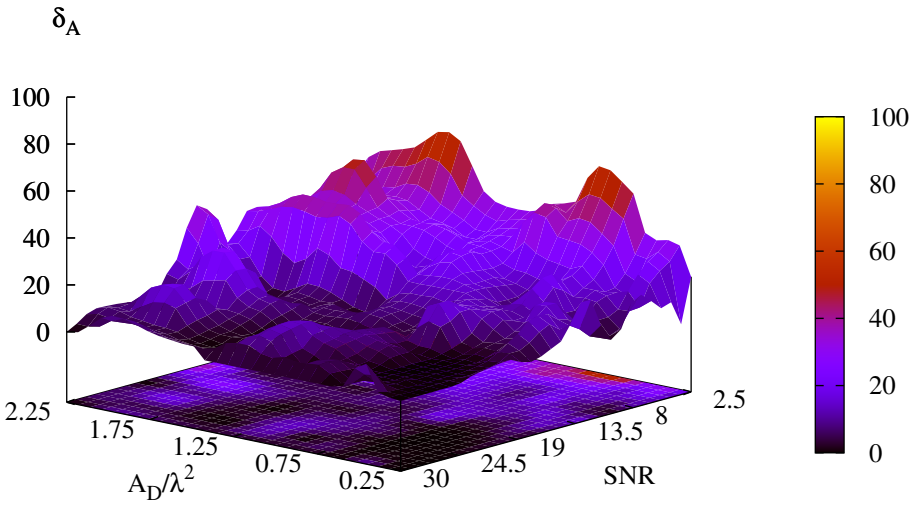

(*c*)

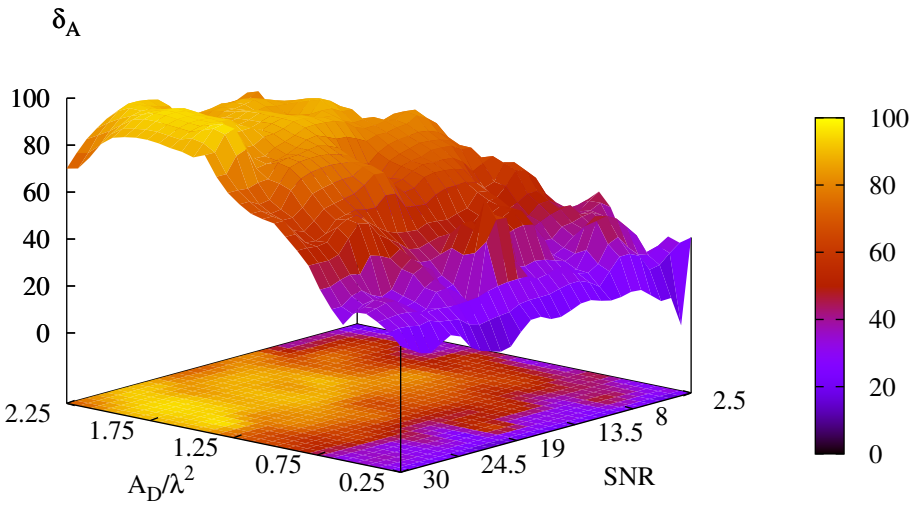

(*d*)

Fig. 3(*II*) - M. Benedetti *et al.*, "Tomographic Sub-Surface Detection ..."

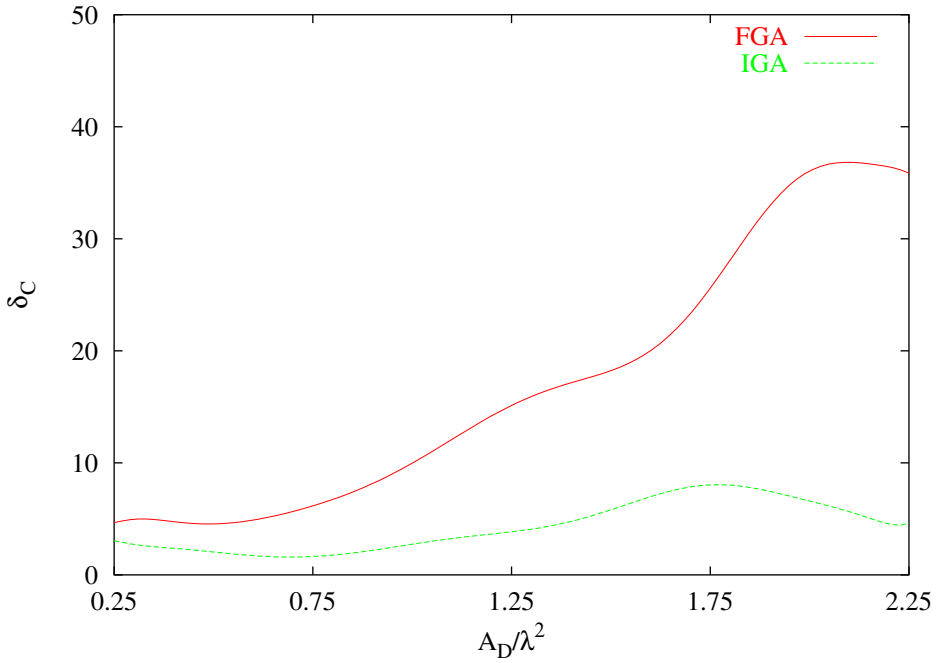

(*e*)

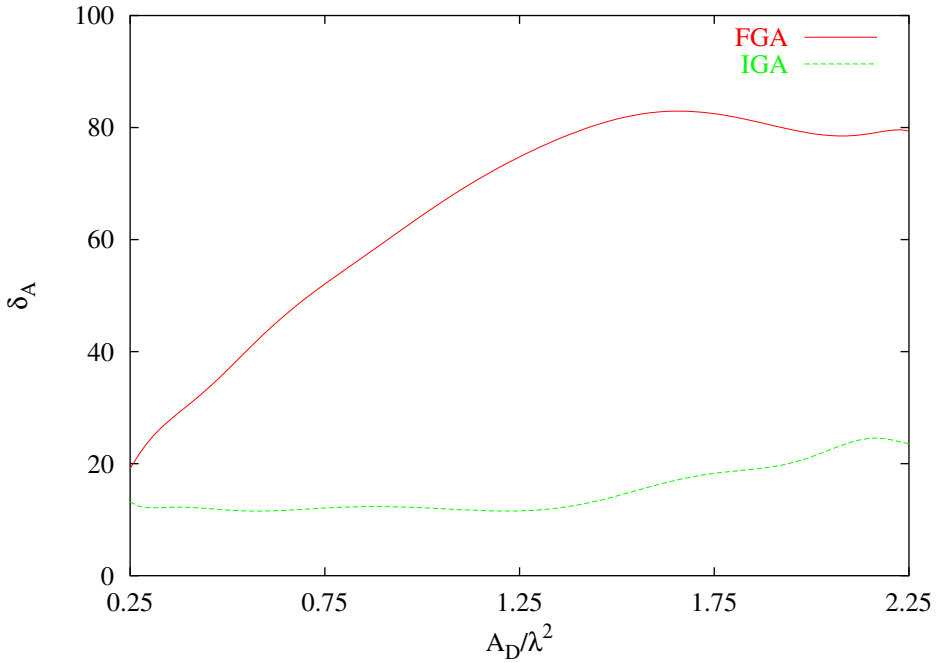

(*f*)

Fig. 3(*III*) - M. Benedetti *et al.*, "Tomographic Sub-Surface Detection ..."

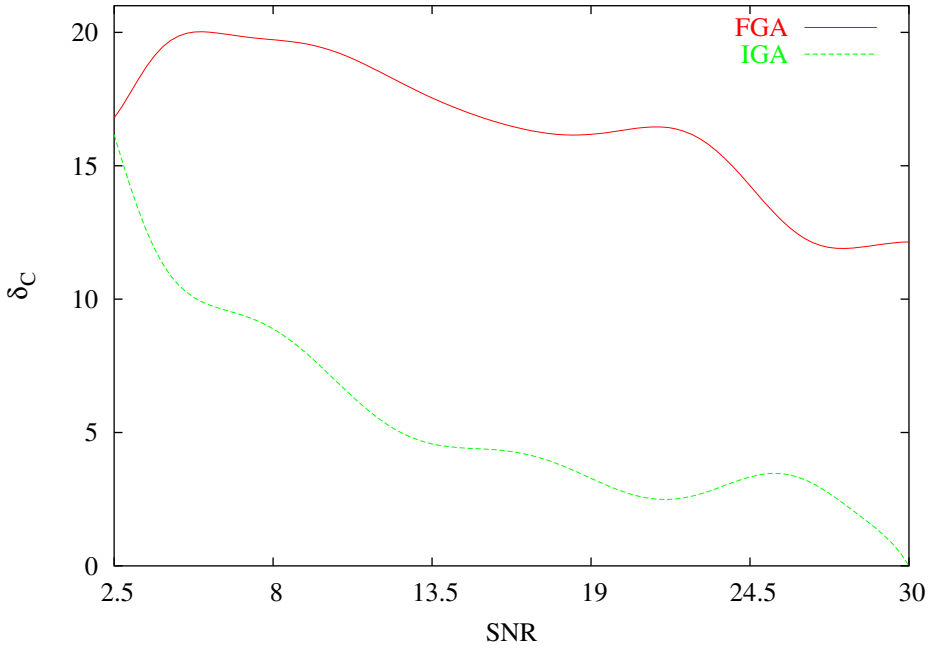

(g)

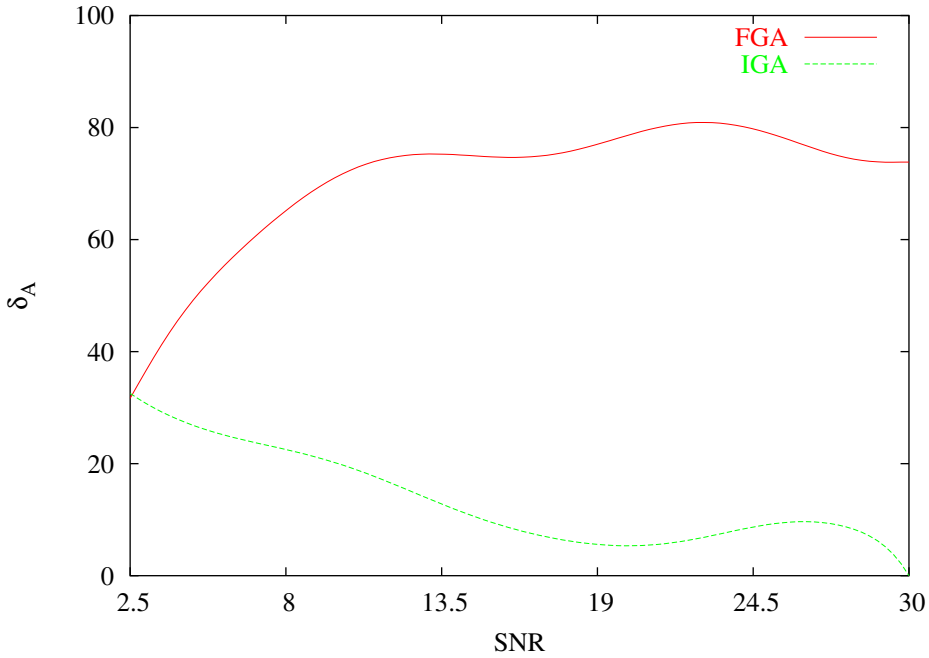

(h)

Fig. 3(IV) - M. Benedetti *et al.,* "Tomographic Sub-Surface Detection ..."

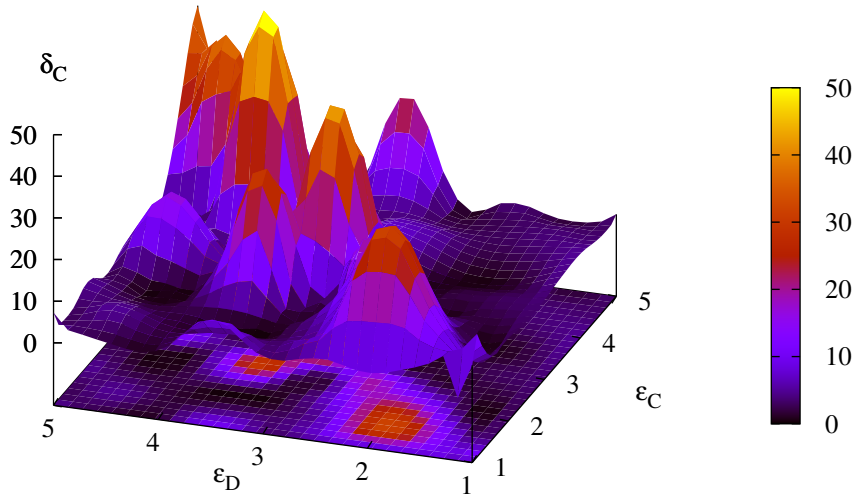

(a)

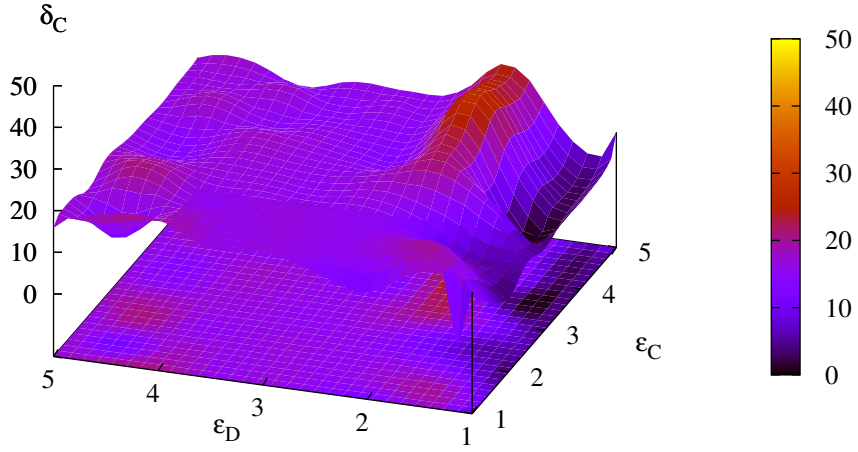

(b)

Fig. 4(I) - M. Benedetti *et al.*, "Tomographic Sub-Surface Detection ..."

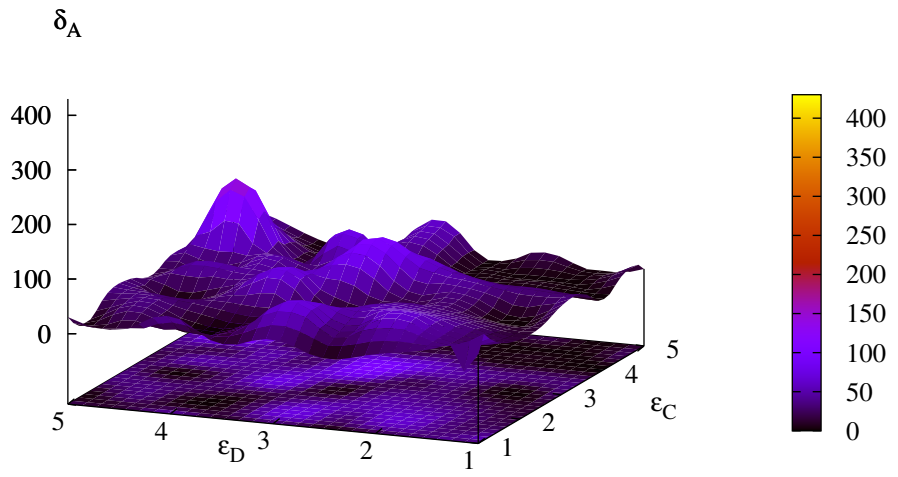

(*c*)

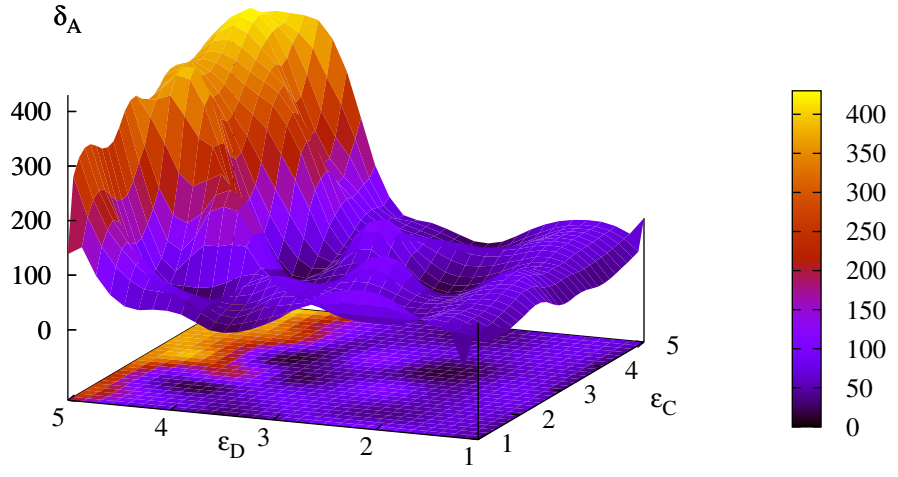

(*d*)

Fig. 4(*II*) - M. Benedetti *et al.*, "Tomographic Sub-Surface Detection ..."

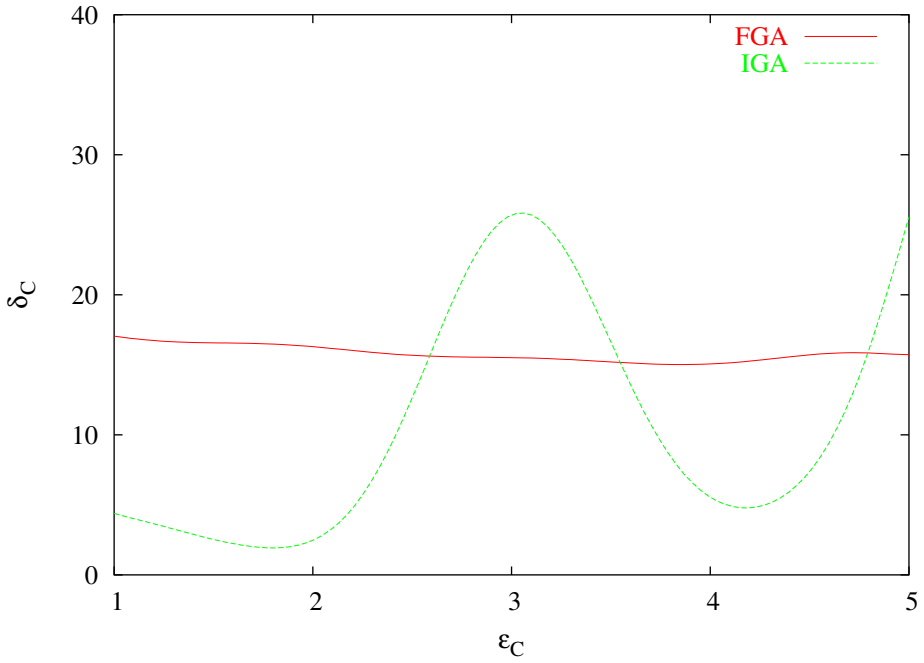

(e)

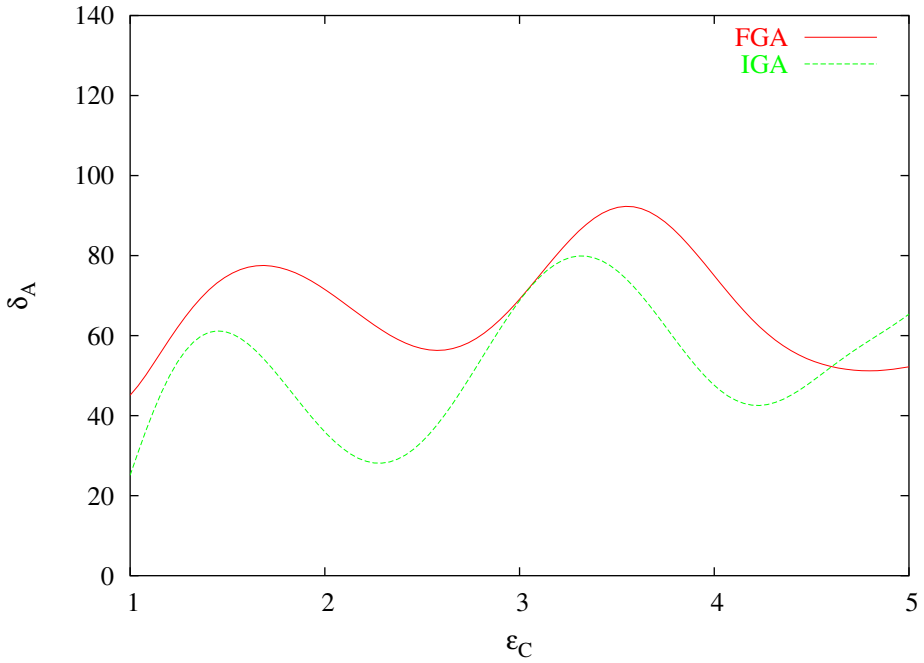

(f)

Fig. 4(*III*) - M. Benedetti *et al.*, "Tomographic Sub-Surface Detection ..."

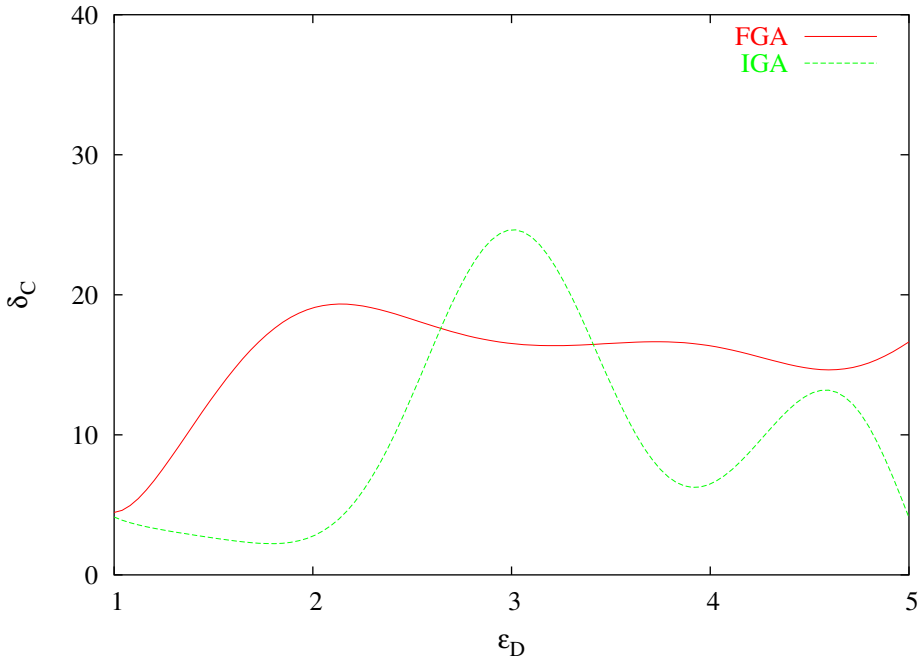

(g)

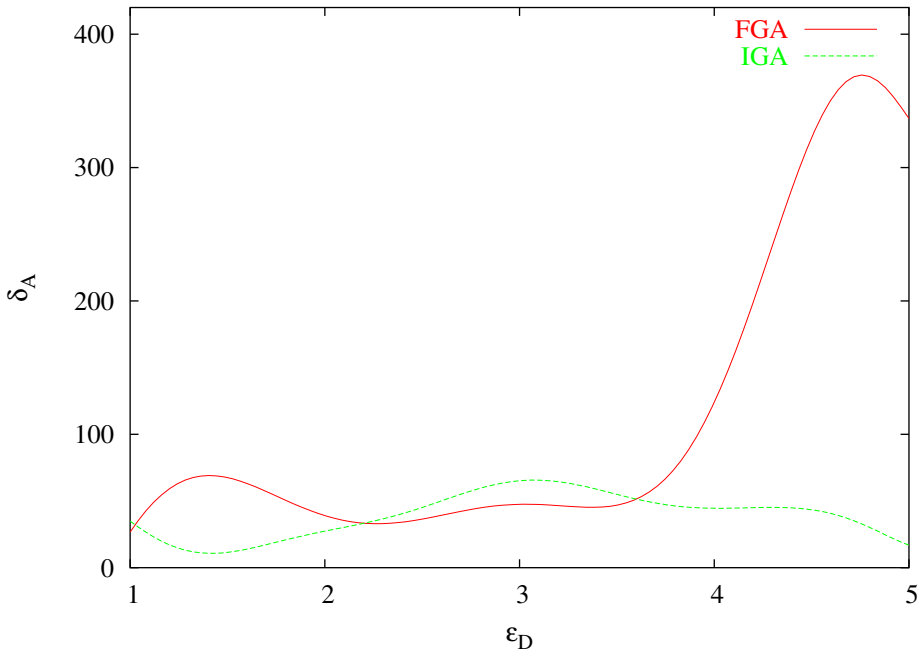

(h)

Fig. 4(IV) - M. Benedetti *et al.*, "Tomographic Sub-Surface Detection ..."

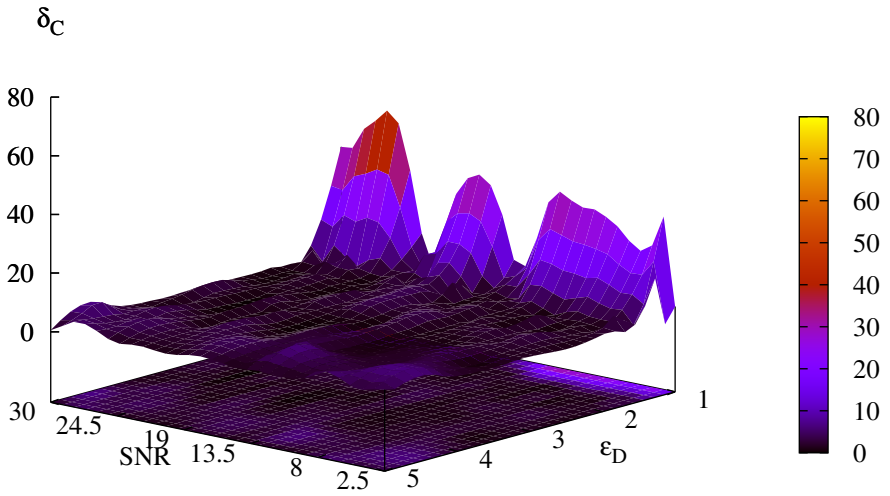

(*a*)

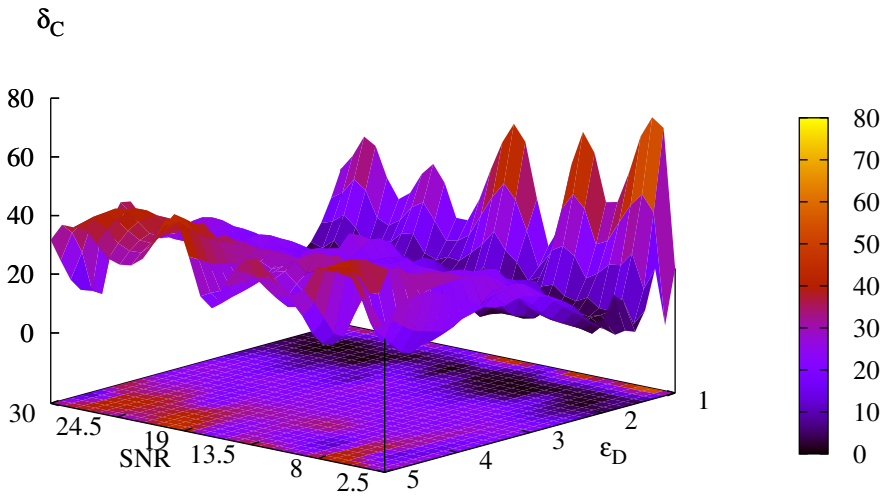

(*b*)

Fig. 5(*I*) - M. Benedetti *et al.*, "Tomographic Sub-Surface Detection ..."

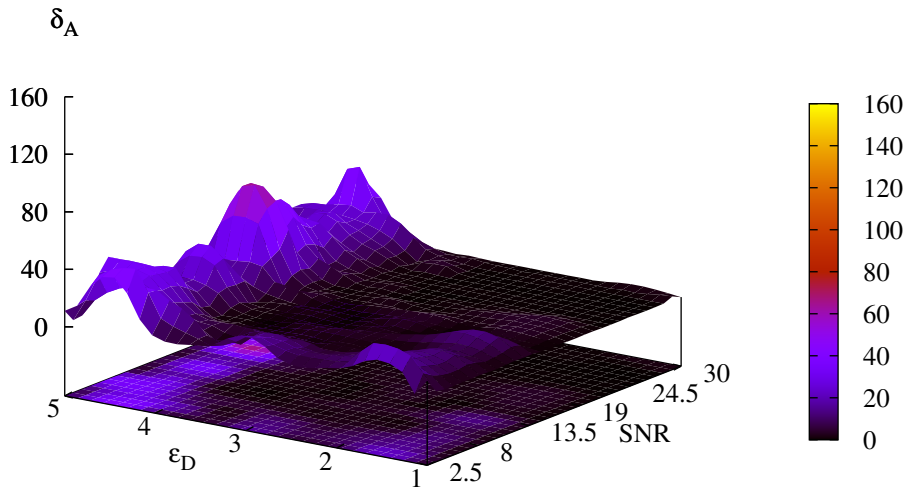

(*c*)

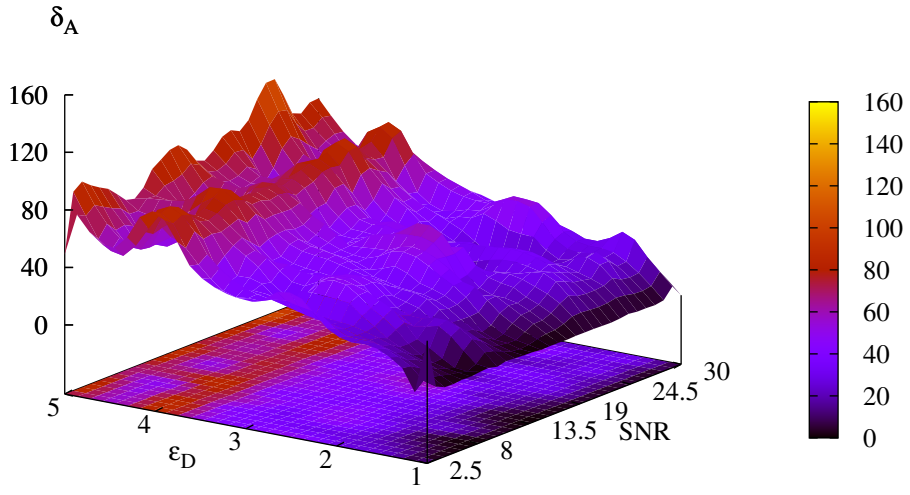

(*d*)

Fig. 5(*II*) - M. Benedetti *et al.*, "Tomographic Sub-Surface Detection ..."

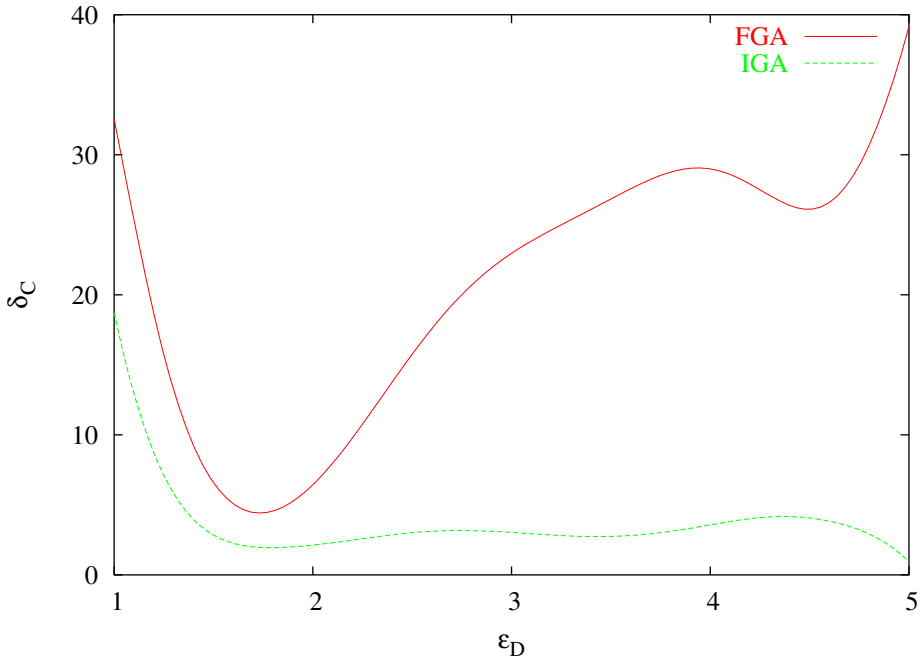

(e)

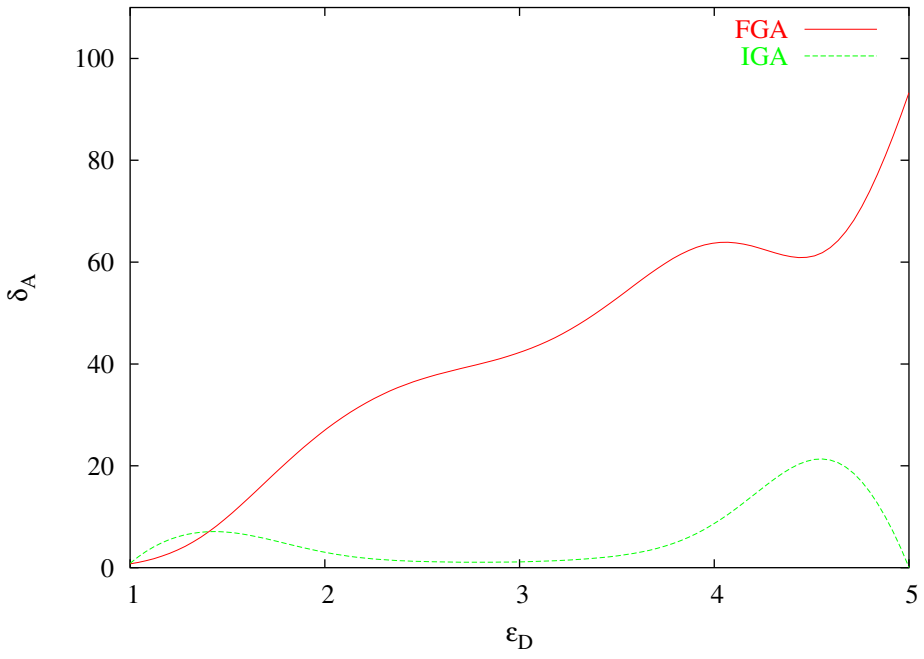

(f)

Fig. 5(*III*) - M. Benedetti *et al.*, "Tomographic Sub-Surface Detection ..."

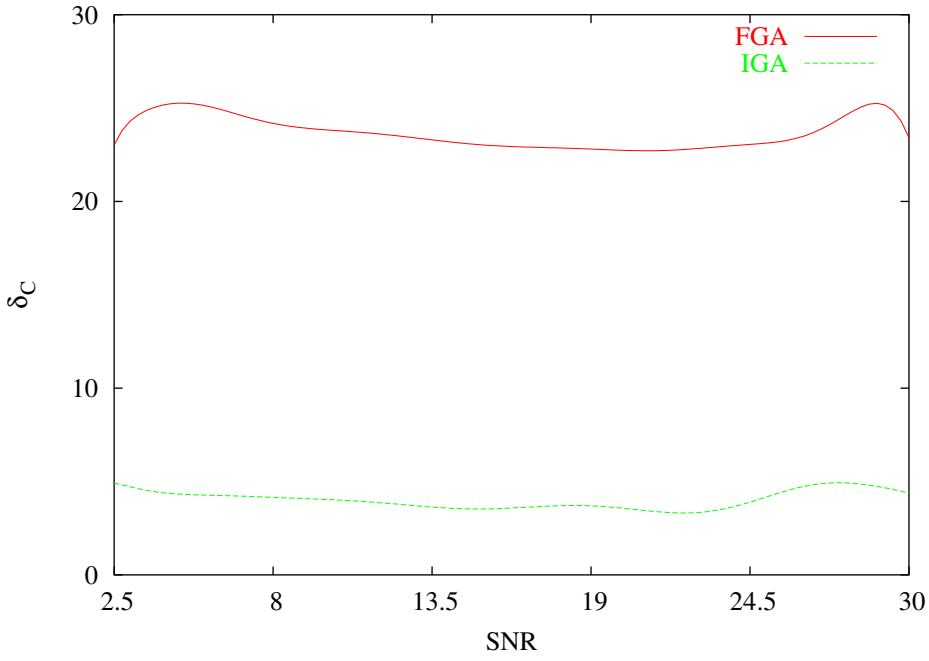

(g)

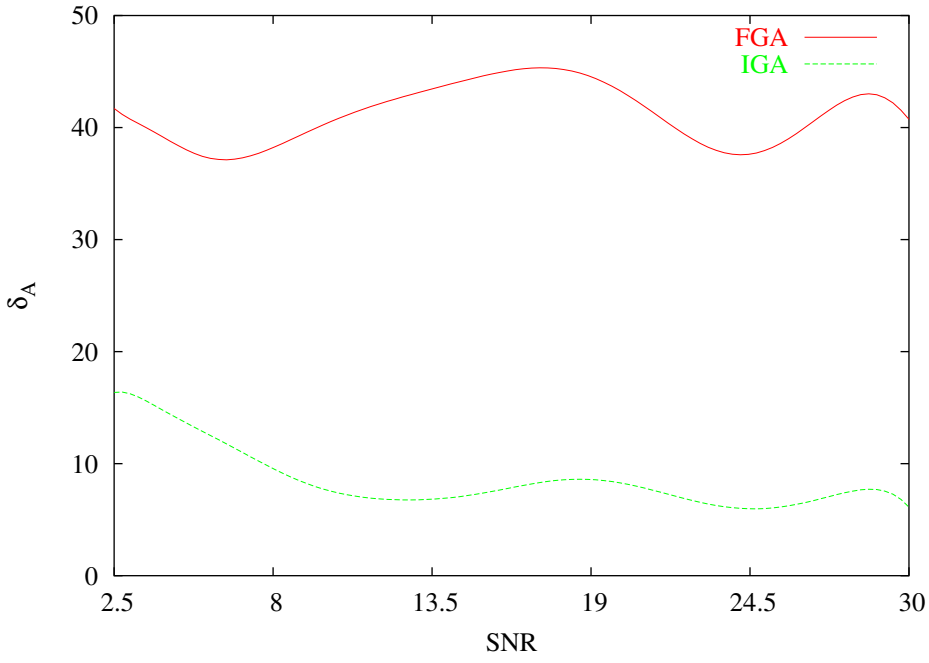

(h)

Fig. 5(IV) - M. Benedetti *et al.,* "Tomographic Sub-Surface Detection ..."

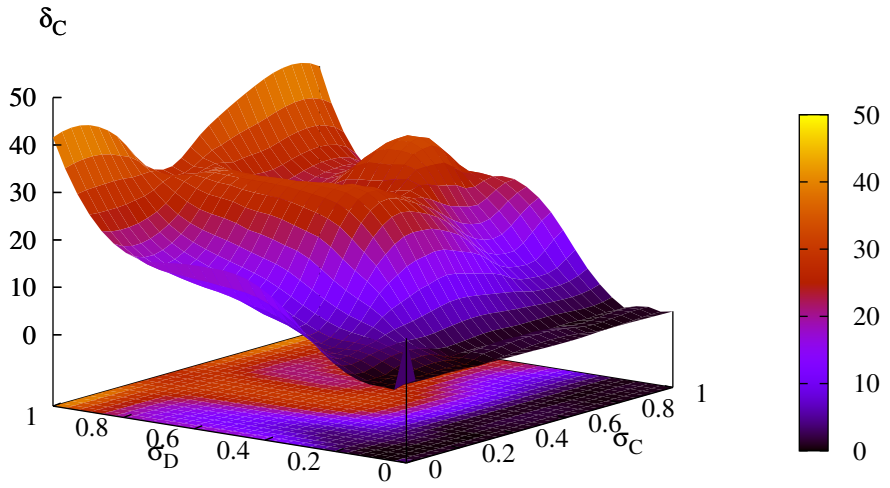

(a)

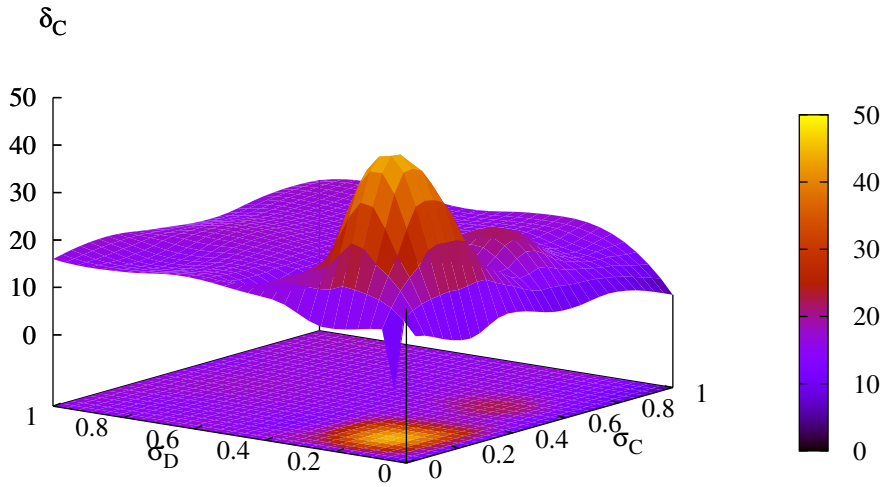

(b)

Fig. 6(I) - M. Benedetti *et al.*, "Tomographic Sub-Surface Detection ..."

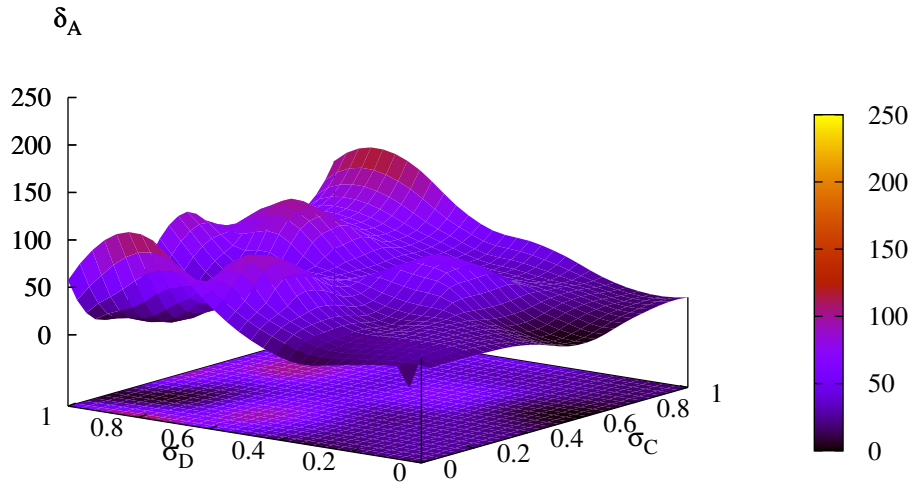

(c)

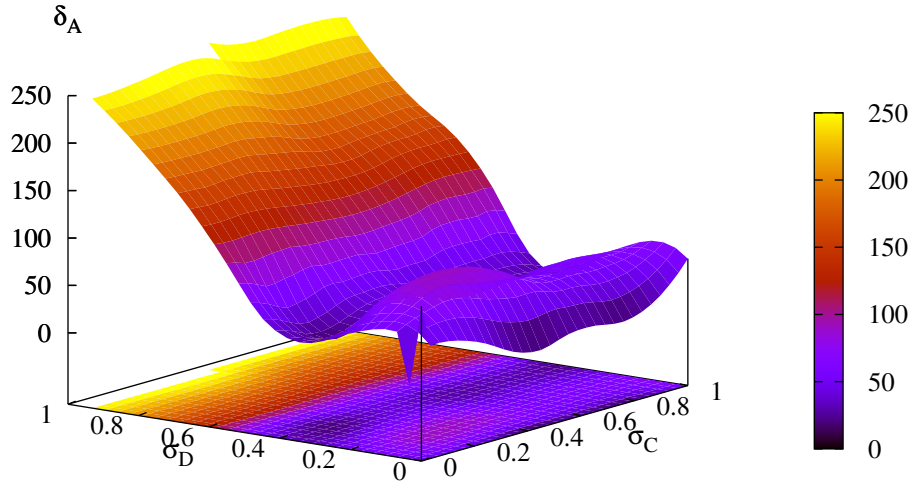

(d)

Fig. 6(*II*) - M. Benedetti *et al.*, "Tomographic Sub-Surface Detection ..."

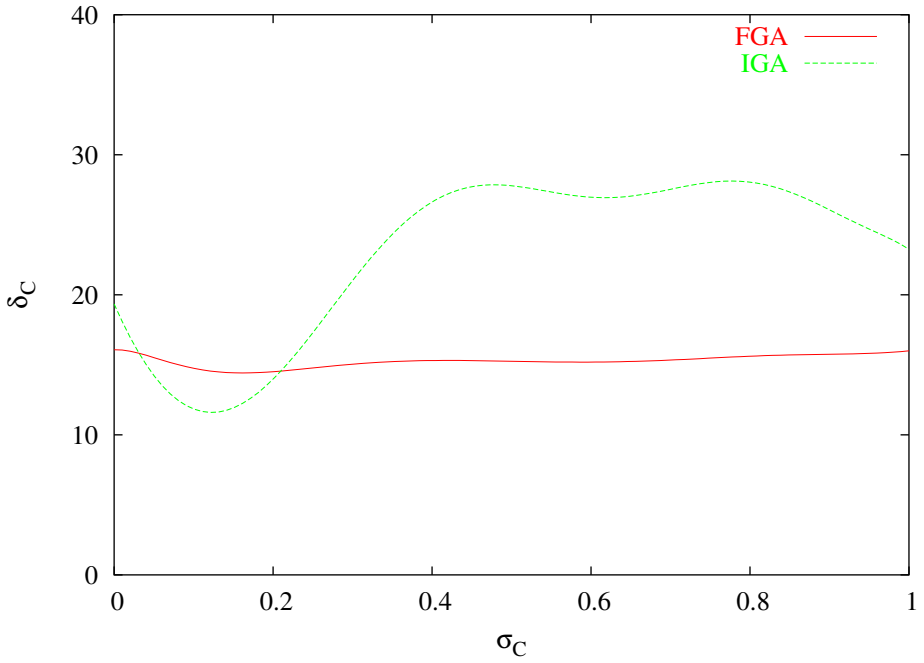

(e)

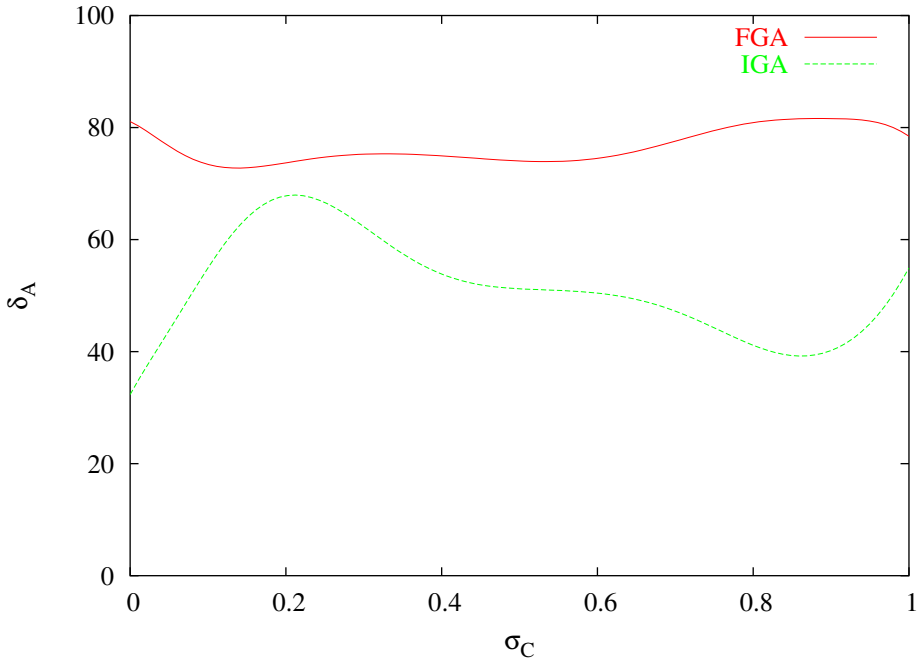

(f)

Fig. 6(*III*) - M. Benedetti *et al.*, "Tomographic Sub-Surface Detection ..."

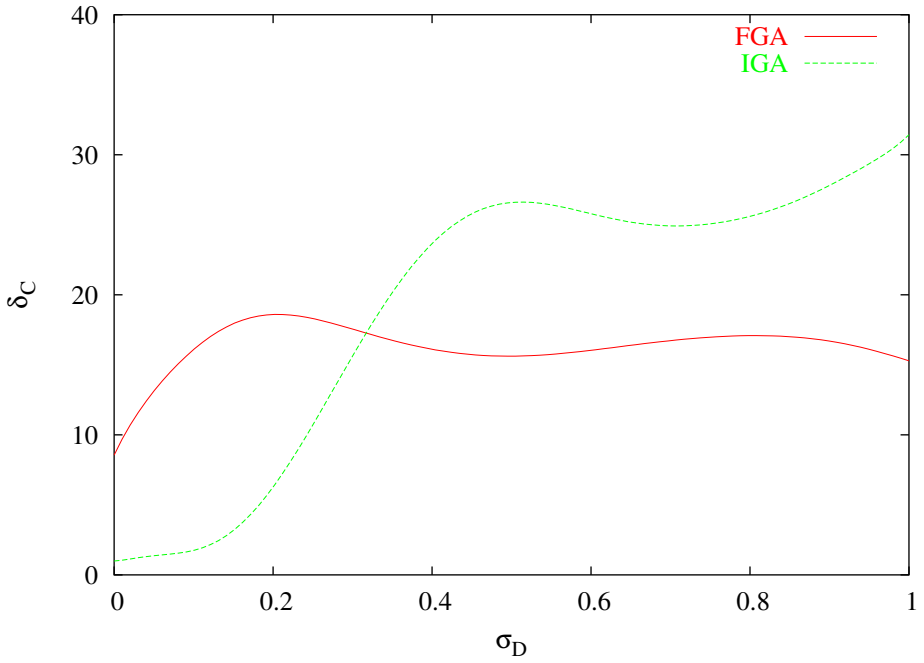

(g)

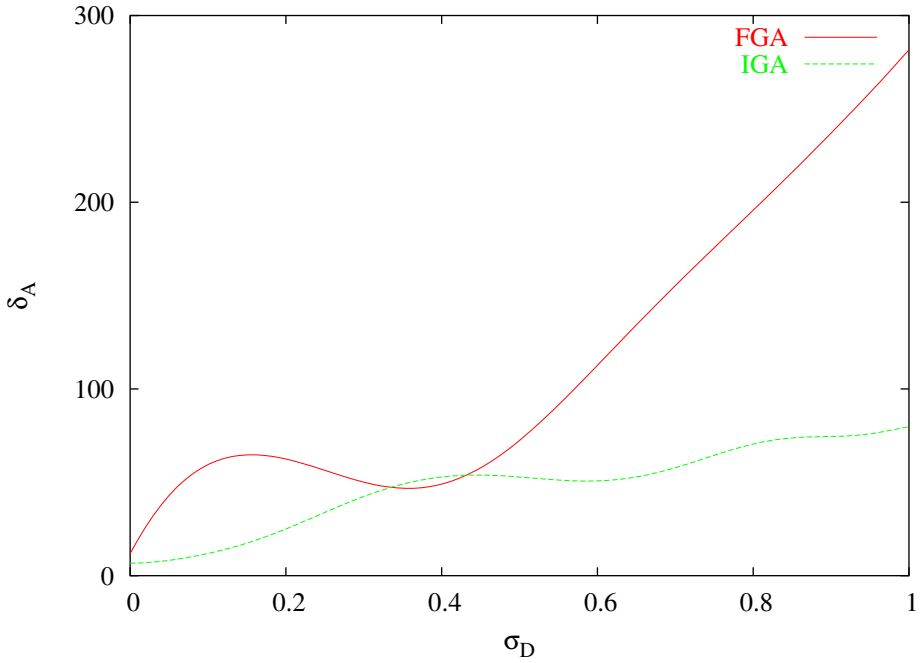

(h)

Fig. 6(IV) - M. Benedetti *et al.,* "Tomographic Sub-Surface Detection ..."

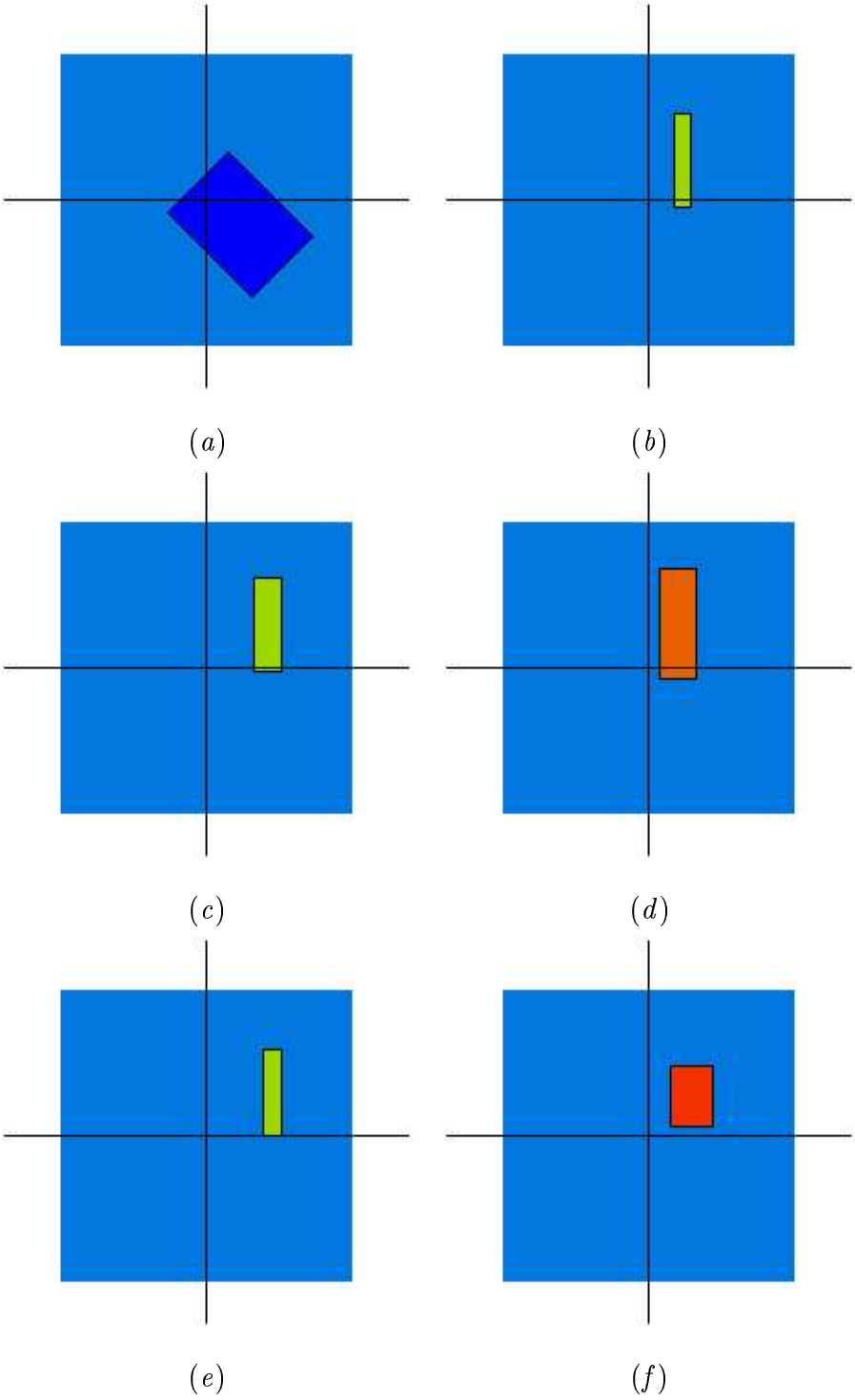

Fig. 7(*I*) - M. Benedetti *et al.*, "Tomographic Sub-Surface Detection ..."

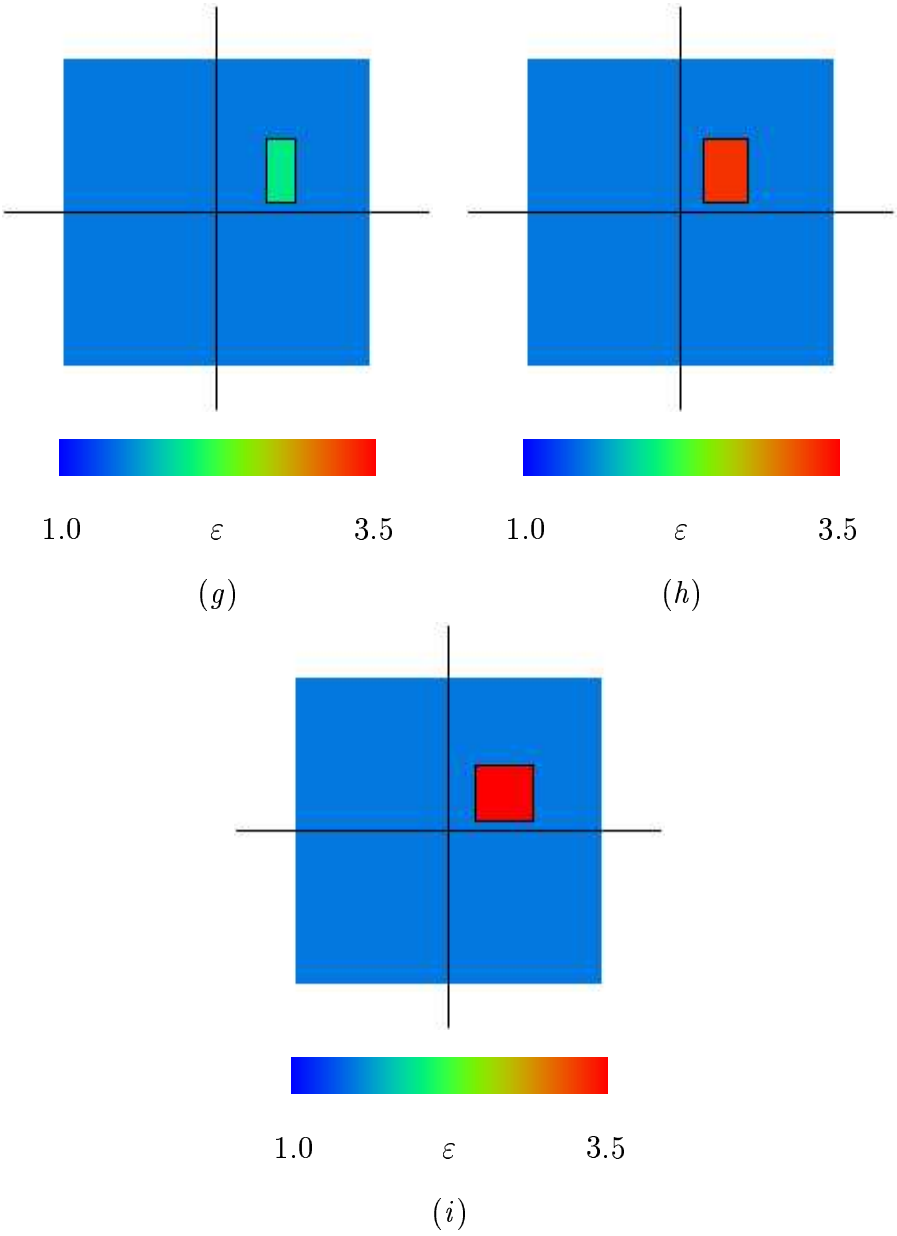

Fig. 7(*II*) - M. Benedetti *et al.*, "Tomographic Sub-Surface Detection ..."